ACP-2015-687

Authors' Responses to Reviewer 2 (anonymous)

Date: 11 June 2016

Title: A numerical study of back-building process in a quasi-stationary rainband with extreme rainfall over northern Taiwan during 11-12 June 2012

Authors: C.-C. Wang, B.-K. Chiou, G. T.-J. Chen, H.-C. Kuo, and C.-H. Liu

The comments from this reviewer (Reviewer 2) and those from other reviewers are appreciated, and the paper has been revised once again according to these comments and suggestions. In this revision, both the roles played by the approaching mei-yu front and the topography of Taiwan are explicitly analyzed and diagnosed, and the forcing of the quasi-linear MCS is also discussed with a newly-added figure. In the revised manuscript (color coded), the changes made in response to Reviewer 2, Reviewer 3, and by ourselves (mostly minor changes in wording or to correct mistakes) are marked in blue, red, and orange, respectively. Our point-by-point responses to each of the comments are listed below, with how and where the revision is made in the text specified.

1. Comment:

This revision did not provide new evidence that can actually address the reviewer's critical concern about the roles of the frontal or topographic forcings in the studied event. Let's take the frontal forcing as an example herein. Specifically, the authors attempted to argue or assume that the frontal forcing was acting at larger scale so it was less relevant to the cell formation at smaller or cloud scale. This strong statement is not convincible in many perspectives. First of all, none of analyses presented can adequately preclude the significant impact of frontal forcings on the initiation of the observed convective cells. As admitted by the authors, both observational and modeling results have shown a very close connection between the frontal forcing and the development of moist convection. In addition, it has been long recognized that, as revealed by numerous mesoscale studies of frontal convection in both mid-latitude and subtropical (like Taiwan) regions (e.g., Carbone 1982, JAS; Trier et al. 1990, MWR; Parson 1992, JAS), the frontal boundary contributing to the initiation or maintenance of moist convection along the leading edge of the synoptic front is mostly acting at convective scale (i.e., meso-gamma) rather than larger scale. Convective cells formed repeatedly near and along the frontal boundary (cf. Figs. 2, 4, 6, and so on) strongly support this scenario. Based on the results discussed in the manuscript, it is generally difficult for the reader to believe that the back-building

process is a sole or important mechanism (at meso-gamma) responsible for the occurrence of heavy precipitation associated with the frontal system.

Reply:

Although they are not the main focus of the present study, we agree with the reviewer that the roles played by the approaching mei-yu front and the topography of Taiwan, as well as how the quasi-linear MCS near northern Taiwan is initiated should be addressed to an adequate extent. Therefore, to discuss these points and also make our paper more complete, a new figure (Fig. 9) is added to show that the rainband in question forms along a near-surface convergence zone (green dotted curves in Fig. 9) between the low-level flow blocked and deflected northward by the topography of Taiwan and the unblocked flow farther to the north and west in the environment (but still ahead of the front, which is marked by black dotted curves in Fig. 9). Thus, the effects of terrain (blocking) played a major role to initiate the development of the quasi-linear MCS, while the front (some 30-90 km to the north) helped provide and channel an enhanced background flow with its approach in the present case. These results are in agreement with and supported by the observations, and a new paragraph under a new title of subsection (Sect. 4.2) is added to discuss the above points (p.12, L15-31; p.20, L8-14; p.32, L7-11; p.46-47), as suggested. Some text in other places are also modified accordingly (p.1, L14 and L23-24; p.8, L19-22; p.10, L27 to p.11, L6).

Also, since the front is shown clearly to be 90-30 km north of the quasi-linear MCS during the entire period of our interests in the newly-added Fig. 9 (as well as in Figs. 2, 4, 6, and 7 in our earlier draft), it plays no direct role in the initiation of the rainband, and the possibility speculated by this reviewer, especially acting locally on the convective scale, can be ruled out. In the revision, some modifications are also performed according to the above findings (p.12, L21-14 and L28-30; p.20, L11-14).

ACP-2015-687

Authors' Responses to Reviewer 3 (anonymous)

Date: 11 June 2016

Title: A numerical study of back-building process in a quasi-stationary rainband with extreme rainfall over northern Taiwan during 11-12 June 2012

Authors: C.-C. Wang, B.-K. Chiou, G. T.-J. Chen, H.-C. Kuo, and C.-H. Liu

The constructive comments from this reviewer (Reviewer 3) are highly appreciated, and the paper has been revised according to these comments and suggestions. Major revisions are made to (1) show that the cold pool is very weak and the cold-pool mechanism plays little role in the development of new back-building cells in the quasi-linear MCS in the present event, (2) address the forcing of the quasi-linear MCS and the roles played by the approaching mei-yu front and the topography of Taiwan in its development, and (3) revise the paper accordingly and remove the vague descriptions (mainly regarding the scale of frontal/terrain forcings). We are happy to have the chance to add these materials and to make the paper more solid and more complete. In the revised manuscript (color coded), the changes made in response to Reviewer 2, Reviewer 3, and by ourselves (mostly minor changes in wording or to correct mistakes) are marked in blue, red, and orange, respectively. The point-by-point responses to each of the general and specific comments are listed below, with how and where the revision is made in the text specified.

1. General comments:

1) In my view, there is insufficient evidence in the paper to support the authors' claim that 'the cold-pool mechanism' was absent in this case. The authors need to point to specific evidence that the cold-pool mechanism was entirely absent in this case. Analyses of near-surface temperature or potential temperature fields could be included in the paper to verify the absence of a surface cold pool in the vicinity of the back building convection. Might it be possible that the initial training line/adjoining stratiform MCS established a cold pool and an associated boundary in the vicinity of northern Taiwan that subsequently served as a focus for the initiation of convective cells within the back-building MCS?

Reply: The reviewer's concern is well taken. To make the paper more complete, a new figure (Fig. 12) is added to show the perturbations in potential temperature (θ') and horizontal winds (u' and v'), and the associated convergence/divergence at the surface during the initiation stage of the back-building cell B2. In this figure, it is confirmed that the cold

pool produced by the old cell B1 is very weak (with θ' of only -0.3 K at most) and is to the east of the updraft, and cannot have played any significant role in the initiation of B2, which is on the rear (opposite) side of B1. A new paragraph is also added to describe and discuss these features related to the figure, as suggested (p.7, L23-24; p.14, L16-29; p.17, L11; p.32, L27 to p.33, L2; p.50). We thank this reviewer for his/her valuable and constructive comments that help improve our paper and make it more complete.

2) The authors provide a very detailed analysis of the various terms of the vertical momentum equation for developing and maturing cells within the back-building convective line. This analysis documents processes associated with the development of convective cells, but it does not explain how the convective cells were actually initiated in the upstream portion of the convective line. It is not clear precisely how the forcing (i.e., lower-tropospheric lifting) necessary to initiate new convective cells in the upstream portion of the convective line was established and how that forcing was manifested. The authors have provided various statements throughout the manuscript vaguely asserting that the convection was linked to forcing related to the approaching front and to low-level convergence associated with terrain-channeled flow without providing any supporting evidence. Moreover, the authors state in the paper, "Given all these driving mechanisms and forcings (at meso-β scale or larger), the BB process at convective (meso-γ) scale was also a contributing factor leading to the extreme rainfall, especially during the later 6 h period after 18:00 UTC" (page 10, lines 8–11). This statement makes it seem as though the back-building process was somehow independent of the forcing at the meso-β scale. Is it possible that the back-building processes was predominantly governed by processes acting at the meso-β scale? Perhaps, new cells developed 15–30 km upstream of old cells simply because that was where lower-tropospheric convergence and lifting were strongest?

Reply: Although they are not the main focus of the present study, we agree with the reviewer that the roles played by the approaching mei-yu front and the topography of Taiwan, as well as how the quasi-linear MCS near northern Taiwan is initiated can and should all be addressed to an adequate extent. Therefore, to discuss these points and also make our paper more complete, a new figure (Fig. 9) is added to show that the rainband in question forms along a near-surface convergence zone (green dotted curves in Fig. 9) between the low-level flow blocked and deflected northward by the topography of Taiwan and the unblocked flow farther to the north and west in the environment (but still ahead of the front, which is marked by black dotted curves in Fig. 9). Thus, the effects of terrain

(blocking) played a major role to initiate the development of the quasi-linear MCS, while the front (some 30-90 km to the north) helped provide and channel an enhanced background flow with its approach in the present case. These results are in agreement with and supported by the observations, and a new paragraph under a new title of subsection (Sect. 4.2) is added to discuss the above points (p.12, L15-31; p.32, L7-11; p.46-47), as suggested. Some modifications are also made throughout the text according to these findings (without vague descriptions) and related efforts (p.1, L14 and L23-24; p.4, L25-26; p.8, L24-26; p.11, L9-11; p.13, L21; p.18, L14; p.19, L8), and we simply state that our focus in this paper is on the BB process at the convective scale (p.4, L20-21; p.11, L5; p.20, L15 and L24). The numbers of later figures are also adjusted throughout the text. Again, we thank this reviewer for his/her valuable and constructive comments that help improve our paper and make it more complete.

3) I suggest including some additional analyses from the CReSS model simulation to illustrate the favorable mesoscale configuration – and the forcing therein – that contributed to new cell development within the back building convective line. For example, you could provide a series of maps showing potential temperature, convergence, and wind on some level in the lower troposphere (e.g., 950 hPa) during the time period of the back building. Such maps could highlight surface boundaries linked to, e.g., convectively generated cold pools or the Mei-yu front, which may have been involved in the development and maintenance of convection.

Reply: Two new figures, one focusing on the development of the quasi-linear MCS and the other focusing on the back-building process of cell B2 to the west of mature cell B1, are added (p.32, L7-11 and L27 to p.33, L2; p.46-47; p.50), very much along the lines as suggested by the reviewer here. Two new paragraphs are also added to discuss the favorable mesoscale configuration – and the forcing therein – that contributed to new cell development within the back building convective line (p.12, L15-31; p.14, L16-29), and they are summarized in our replies to major comments #1 and #2 above.

4) Somewhere in the introduction, please provide a brief description of the Mei-yu season and how extreme precipitation can be produced in connection with the Mei-yu front. Such information would likely be useful for readers who are unfamiliar with the meteorology of southeastern Asia.

Reply: In the revision, a brief description of the mei-yu season and how heavy rainfall can be produced in connection with the mei-yu front and the LLJ is added in the introduction

section with appropriate references, as suggested (p.3, L16-21; p.4, L9; p.23, L13-15 and L18-19; p.24, L4-6; p.25, L10-11). Thank you for this nice suggestion.

5) The impact and scientific significance of the paper would be enhanced if the authors were to include a discussion of how the results of their study relate to those of prior studies of back-building MCSs. Such a discussion could help to put the results of this study into a broader context and to emphasize the implications and importance of the results.

Reply: In the revision, the difference and new findings of the present study are better emphasized in the abstract, text body, and the conclusion, alone the lines as suggested (p.1, L16-18; p.2, L4-5; p.21, L10-12). We thank this reviewer for this nice suggestion.

2. Specific comments:

1) P1,L14: What do you mean by 'across the scale'? Which scale specifically?

Reply: In the revision, since the background forcing for the development of the quasi-linear MCS is diagnosed in Sect. 4.2, as replied to major comment #2 above, there is no need to mention the specific scale here and the sentence in question is revised to "In the midst of background forcing of low-level convergence, the back-building (BB) process …", along the lines as suggested (p.1, L14-15).

2) P1,L17: What do you mean by 'more favorable'? More favorable than what?

Reply: In the revision, it is clarified that we mean that the location about 15-30 km upstream from the old cell is still often more favorable for new cell initiation than other places in the MCS, as suggested (p.1, L19-20).

3) P2,L2: Perhaps better to say 'location' rather than 'spot'.

Reply: Revised as suggested (p.2, L4).

4) P2,L6: Consider inserting 'convective' after organized.

Reply: Since the term mesoscale convective systems (MCSs) just appears a few words before, to add "convective" here may be a bit repetitive and therefore the text remains not changed (p.2, L9).

5) P2,L23: 'upwind' is ambiguous here; perhaps you mean 'upstream relative to the system motion vector'.

Reply: The word "upwind" is replaced by "upstream" here, along the lines as suggested. The whole sentence reads "In BB lines, new cells form repeatedly on the upstream side at nearly the same location then move downstream, making the line as a whole almost stationary" and should be already clear that the new cells form on the upstream side relative to their motion vector after formation (p.2, L26-27).

6) P2,L25: The authors seem to imply here that TL/AS and BB MCSs are completely distinct. In fact, there is often overlap between these two types of MCSs. Heavy-rain-producing MCSs can often feature characteristics of both types. Case studies by Schumacher et al. (2011) and Peters and Schumacher (2015) illustrate this.

Reply: In the revision, it is noted that some MCSs may possess characteristics of both types, and the references of Schumacher et al. (2011) and Peters and Schumacher (2015) are both cited, as suggested (p.2, L28-30; p.27, L6-8).

7) P2, L27-30: Back building of convection can also occur in conjunction with lifting along a quasi-stationary frontal boundary as well (e.g., Schumacher et al. 2011).

Reply: This possibility is added in the revision with reference to Schumacher et al. (2011), as suggested (p.2, L31 to p.3, L4; p.27, L6-8).

8) P3,L11-14: Although environments in the tropics and subtropics may not always be conducive to the formation of strong surface cold pools in association with convection, cold pools can often develop in conjunction with subtropical and tropical MCSs and can often play an important role in MCS organization and evolution. Also, cold pools need not be strong in order to impact the evolution of an MCS. In my view, it is erroneous to downplay the importance of cold pools in subtropical and tropical MCSs.

Reply: The sentence is revised to simply state that strong cold pools are not required in some BB systems in Taiwan (and some other subtropical regions), as suggested (p.3, L22-24). As mentioned earlier in the manuscript, some events in the East Asia are caused by the cold pool mechanism as similar to in many mid-latitude systems (p.3, L4-5), so we do

not downplay the importance of cold pools.

9) P4,L10: What do you mean by 'across the scale'? Which scale specifically?

Reply: This sentence is revised to be more specific and remove the portion "across the scale" to avoid ambiguity or confusion, as suggested (p.4, L19-20). Later in the text, the other factors linked to frontal forcing and topographic effects are explicitly discussed in Sect. 4.2 (please see our reply to major comment #2 above).

10) P4,L28: Replace 'resulted' with 'resulting'.

Reply: Revised as suggested (p.5, L9).

11) P6,L14-15: More precisely, positive (negative) values of a laplacian of some variable correspond to local minima (maxima) of that variable, right?

Reply: The sentence is revised to "… a positive (negative) center in $\nabla^2 p'$ corresponds to a local minimum (maximum) in p' itself" to be more precise, as suggested (p.7, L1-2).

12) P7,L17: Here and elsewhere in the paper, how were frontal positions determined?

Reply: In the revision, it is clarified that the frontal position is mainly determined based on wind fields, since the mei-yu front near Taiwan is often associated with strong cyclonic shear vorticity but only weak thermal contrast (p.8, L7-10), as suggested. A few references are also cited to support this notion (p.23, L20-21; p.26, L8-9; p.28, L6-7).

13) P7,L20: Replace 'as well as' with 'as does'.

Reply: The sentence is rearranged, and the corresponding portion is revised to "as is the ASCAT observation" similar to suggested (p.8, L10-13).

14) P7,L22: Insert 'possibly' before 'produced'.

Reply: This sentence here is revised to "Such a configuration is often produced…" with the supporting references cited (p.8, L16-19; p.28, L3-4).

15) P7,L24: I am really confused. I do not understand physically how moisture flux

convergence can influence the formation of the near-surface wind pattern in Fig. 2a. Please explain. Also, although moisture flux convergence is mentioned multiple times in the paper, the authors do not actually show moisture flux convergence calculations.

Reply: Here, the description about how terrain blocking can result in formation of local barrier jets near the tips of Taiwan when the prevailing flow intensifies, and how the convergence associated with the one near northern Taiwan can provide the forcing for quasi-linear MCSs in the region is revised with better clarity (p.8, L15-22; p.28, L3-4). We agree with the reviewer that there is no need to mention "moisture flux convergence" here, so this terminology is removed from the description, as suggested (p.8, L17-18).

16) P7,L25-26: This statement is vague. How exactly is this pattern 'particularly conducive'? Please explain.

Reply: The related description is revised to be more specific, as suggested (p.8, L19-22). Since a new figure (Fig. 9) is added to clarify the formation mechanism of the quasi-linear MCSs near northern Taiwan in Sect. 4.2, here we only state that "the low-level convergence (from confluence) associated with the barrier jet can provide the forcing for quasi-linear MCSs near or south of the front" near northern Taiwan (p.8, L19-22).

17) P8,L5-6: There is no antecedent for 'the barrier jet'. Which barrier jet?

Reply: In the revision, the barrier jet is introduced and explained earlier in the text, as suggested (p.8, L15-22 and L29; p.11, L21).

18) P8,L12: Note, however, that the sounding indicates that the environment is subsaturated; perhaps this suggests the possibility for cold pool formation?

Reply: In the revision, it is clarified here that the temperature lapse rate near the surface (below 925 hPa) was close to dry adiabats (p.8, L30 to p.9, L1), and thus gives no sign of a cold pool. More importantly (and directly in clarifying the concern), in Sect. 4.3, a second new figure (Fig. 12) is added following the suggestion to show that the cold pool (very weak and to the east of old cell B1) essentially plays no role in the initiation of back-building cell B2 (to the west of B1) in our simulation (p.14, L16-29). Please also see the replies to major comments #1 and #3 above.

19) P9, L21: What is meant by 'more active' here?

Reply: The sentence is revised and the wording of "more active" is removed, along the lines as suggested (p.10, L15-17).

20) P10,L2-6: In my view, you have not shown sufficient evidence to support this statement. Also, it is not clear what is meant by 'forcings of the approaching front as well as the terrain-influenced low-level convergence and moisture flux convergence', nor is it clear how such forcings were related to the development and maintenance of convection. The authors have not provided any diagnostics to quantify frontal or terrain-influenced forcing.

Reply: In the revision, a new figure (Fig. 9) is added to discuss and clarify the formation mechanism of the quasi-linear MCSs (the second one in specific) and the roles played by both the mei-yu front and the topography in our model results (in Sect. 4.2), which are highly consistent with the observations, as suggested (p.12, L15-31). Thus, the materials here (near the end of Sect. 3) is revised accordingly, and there is no need to mention (or assume) the scale of the forcings by the front and/or topography (p.10, L27 to p.11, L11). Please also see the replies to major comment #2 above.

21) P11,L30: 'observations' instead of 'observation'.

Reply: Corrected as suggested (p.13, L9).

22) P12,L19-20: What is meant by 'forcings of the front and terrain' and how were these forcings favorable for new cell development?

Reply: The related description here is clarified that the structure with near-surface convergence is clearly favorable for upstream development of new cells, and the newly-added discussion in Sect. 4.2 is also referenced, as suggested (p.13, L29 to p.14, L2).

23) P12,L22-24: The authors describe the acceleration and deceleration of the LLJ in Fig. 10b, which to me implies that the wind within the LLJ is changing with respect to time. This is, however, not shown in Fig. 10b. Rather, Fig. 10b shows spatial variations of the wind at a single time. Please revise.

Reply: The reviewer is correct that Fig. 11b (Fig. 10b previously) shows spatial variation of

8

the (low-level) wind at a single time. In the case here, the conversion between space and time, as used in the description, is valid under two conditions: (1) a quasi-steady state can be assumed (i.e., the spatial pattern does not change rapidly with time) and (2) the cross section is along the flow (so the air parcels would stay on the section plane during their motion). One widely-accepted example is in the description of air parcel acceleration and deceleration as it passes through the jet core of a straight-line upper-level jet streak, also using a wind pattern of the jet streak at a single time (but in a quasi-steady state). As both conditions are also met in our case here, in the revision, the two conditions are added into the description for better clarity, as suggested (p.14, L2-5).

24) P13,L18: Replace 'details' with 'detail'.

Reply: Replaced as suggested (p.15, L12).

25) P14,L24: It is not accurate to say that moisture flux convergence drives MCS development. My understanding is that moisture flux convergence is 'associated with' or 'a signature of' MCS development.

Reply: For all MCSs in general, we agree with the reviewer that they are associated with convergence (and thus moisture flux convergence) at low levels. However, for those that are driven by low-level convergence from below, as in the present case here, the sentence does not appear problematic. In any case, since we have explicitly discussed the driving mechanism for the MCS in Sect. 4.2 (p.12, L15-31) and the reference to "moisture flux convergence" is not really necessary, the sentence here is revised to "… suggesting the importance of near-surface convergence in driving the development of the line-shaped MCS in this event, as also shown earlier in Sect. 4.2 (and cf. Fig. 11a)" for better clarity (p.16, L18-19).

26) P14,L26–P15,L2: I find the reasoning in these lines of text to be difficult to follow. Please clarify.

Reply: The material in this paragraph is revised to be more specific and with explicit reference to the method employed following Wang et al. (2015), as suggested (p.16, L20-27).

27) P15,L10-11: If the downdraft regions are characterized by positive buoyancy, how are the downdrafts being forced?

Reply: The downdrafts at the flanks are forced from above at higher levels (due to both adiabatic/evaporative cooling and loading of condensates, with $B < 0$), and they reduce in strength during sinking (since $B > 0$). The time evolution (weakening) of downdrafts from 20:00 to 20:20 UTC (cf. Fig. 15a and d) is also consistent with $B > 0$. In the revision, it is clarified that the downdrafts originate at higher levels (p.17, L4-5), as suggested.

28) P15,L19: According to eq. 2, changes in buoyancy are largely governed by changes in θ_v'. Given that changes in θ_v' can only arise due to diabatic processes (e.g., latent heating, evaporative cooling), it is not clear to me how adiabatic cooling or warming can result in buoyancy changes. Please explain.

Reply: The reviewer is correct that changes in θ_v' of an air parcel can only arise from diabatic processes following its trajectory from the Lagrangian perspective. The discussion on the buoyancy change here in the vertical cross-sections, however, is from the Eulerian perspective (i.e., local change) and also has the adiabatic effect associated with vertical motion (or stability term). For example, adiabatic cooling (in T) associated with rising motion contributes to local minimum in θ (and θ_v) in a stable atmosphere ($\partial\theta/\partial z < 0$) since the air coming from below (following dry adiabatic ascent) has a lower θ than the original environment. Therefore, the description here should be OK and remains unchanged (p.17, L11-14).

29) P15,L25: Is melting of hydrometeors not important in this case?

Reply: For the discussion here (at about 3 km), the melting is not important as the melting level (level of 0°C) is at about 5 km (cf. Fig. 3) and much higher. Since the melting effect has little relevancy to the discussion here, the text is not changed (p.17, L18-19). Please also see our reply to specific comment #30 below.

30) P17,L6: Perhaps this is a naive question, but are other diabatic processes (e.g., radiation, melting) unimportant here?

Reply: As explained above in our reply to specific comment #29, the melting level is at about 5 km and much higher than our area of discussion (mostly at low levels), and the latent heat of melting is only a fraction of that of vaporization (and seems too minor). We do, however, indicate that the strength of the rear-flank downdraft can be sensitive to the cloud microphysical scheme at the end of the paragraph (p.17, L22-25).Also, cloud radiation is not parameterized (not included) in CReSS as described in Sect. 2.2 (p.5,

L19-22), so it could not have an effect in the model.

31) P17,L21-22: Insert 'possibly' before 'enhanced'; the authors have not explicitly shown that evaporative cooling was involved.

Reply: The word "likely" is inserted here, along the lines as suggested (p.19, L16).

32) P17,L29-30: Even without the 'three advantages' associated with a nearby cell, C1 still appears to develop into an intense convective cell (Fig. 9). Perhaps this suggests other factors are more important for convective cell development?

Reply: Indeed, cell C1 develops even without the "three advantages" identified to come from the nearby mature cell, and this is noted in the text at several places (p.4, L26-27; p.18, L13-16; p.20, L26-28). In the paper, there is no deny in the importance of the background forcing of near-surface convergence as shown in Sect. 4.2, but by comparing B1-B2 pair with C1, we can identify the additional factors that work in synergy with other existing factors and help initiate the new convection of B2 (and thus the BB process). This point is also stated in multiple places in the paper (p.1, L14 and L23-24; p.4, L26-27; p.10, L27-29; p.14, L4; p.18, L13-16; p.19, L7-11; p.20, L23-24 and L26-28).

33) P18,L12-13: Again, in my view there is insufficient evidence to support this claim.

Reply: In the revision, evidence is provided to support the claim that the cold pool mechanism is not responsible for the triggering of new BB cells in the present case (Sect. 4.3; p.14, L16-29), as in our reply to major comment #1 (and #3) above. The description here is revised also in response to the major comment #5 to better emphasize the difference in this study from past efforts, as suggested (p.20, L3-7).

34) P18,L22-23: There is insufficient evidence to support this statement. The authors have not provided any diagnostics to quantify frontal or terrain-influenced forcing.

Reply: The background forcing for the development of the quasi-linear MCS is diagnosed in the revision in Sect. 4.2 (p.12, L15-31), as in our reply to major comment #2 above. A new paragraph above is added to summarize the relevant result (p.20, L8-14), along the lines as suggested, and therefore the description here is shortened (p.20, L23).

35) P18,L28: It seems to me that the old cell may have influenced the development

of the new cell but did not play a role in the actual triggering/initiation of the new cell.

Reply: The three identified advantages from the old cell all have positive influences on the development of new cell B2 about 15-30 km upstream, and thus are contributing factors and helpful to the triggering/initiation of the new cell at that location. Since all the factors (including the background forcing of convergence) work together in synergy to trigger B2 in the model, it is very difficult to say for sure that the new BB cell would or would not be triggered if the old cell B1 were not there, but the process would definitely be slower without the presence of B1 in the case where B2 is eventually triggered (as shown in Sect. 5 through comparison). The description here is slightly modified, along the lines as suggested (p.20, L26-28).

References:

Schumacher, R. S., T. J. Galarneau Jr., and L. F. Bosart, 2011: Distant effects of a recurving tropical cyclones on rainfall in a midlatitude convective system: A high-impact predecessor rain event. *Mon. Wea. Rev.*, **139**, 650-667, doi:10.1175/2010MWR3453.1.

Peters, J. M., and R. S. Schumacher, 2015: Mechanisms for organization and echo training in a flash-flood-producing mesoscale convective system. *Mon. Wea. Rev.*, **143**, 1056-1083, doi:10.1175/MWR-D-14-00070.1.

A numerical study of back-building process in a quasi-stationary rainband with extreme rainfall over northern Taiwan during 11-12 June 2012

C.-C. Wang[1], B.-K. Chiou[1], G. T.-J. Chen[2], H.-C. Kuo[2], and C.-H. Liu[3]

[1] Department of Earth Sciences, National Taiwan Normal University, Taipei, Taiwan

[2] Department of Atmospheric Sciences, National Taiwan University, Taipei, Taiwan

[3] Department of Atmospheric Sciences, Chinese Culture University, Taipei, Taiwan

Correspondence to: C.-C. Wang (cwang@ntnu.edu.tw)

Abstract

During 11-12 June 2012, quasi-stationary linear mesoscale convective systems (MCSs) developed near northern Taiwan and produced extreme rainfall up to 510 mm and severe flooding in Taipei. In the midst of background forcing of low-level convergence, the back-building (BB) process in these MCSs contributed to the extreme rainfall, and thus is investigated using a cloud-resolving model in the case study here. Specifically, as the cold pool mechanism is not responsible for the triggering of new BB cells in this subtropical event during the mei-yu season, we seek answers to the question why the location about 15-30 km upstream from the old cell is still often more favorable for new cell initiation than other places in the MCS.

With a horizontal grid size of 1.5 km, the linear MCS and the BB process in this case are successfully reproduced, and are found to be influenced more by the thermodynamic and less by dynamic effects. During initiation in a background with convective instability and near-surface convergence, new cells are associated with positive (negative) buoyancy below (above) due to latent heating (adiabatic cooling), which represent a gradual destabilization. At the beginning, the new development is close to the old convection, which provides stronger warming below and additional cooling at mid-levels from evaporation of condensates in the downdraft at the rear flank, thus yielding a more rapid destabilization. This enhanced upward

decrease in buoyancy at low levels eventually creates an upward perturbation pressure gradient force to drive further development along with the positive buoyancy itself. After the new cell has gained sufficient strength, the old cell's rear-flank downdraft also acts to separate the new cell to about 20 km upstream. Therefore, the advantages of the location in the BB process can be explained even without the lifting at the leading edge of the cold outflow.

1 Introduction

As a common type of mesoscale convective systems (MCSs) with a lifespan around 3-12 h, organized rainbands such as squall lines are capable of producing persistent precipitation at high intensity, compared to ordinary, isolated, or scattered convection (e.g., Carbone, 1982; Bluestein and Jain, 1985; Rotunno et al., 1988; Browning, 1990; Houze et al., 1990; Chen and Chou, 1993; LeMone et al., 1998; Parker and Johnson, 2000; Doswell, 2001; Johnson and Mapes, 2001; Sun and Lee, 2002; Weisman and Rotunno, 2004; Meng et al., 2013). When such rainbands are slow-moving and the embedded deep convective cells travel at small angles almost parallel to the line, multiple cells can pass through the same locations in succession to rapidly increase rainfall accumulation and the potential for flash floods (e.g., Maddox et al., 1979; Doswell et al., 1996; Brooks and Stensrud, 2000; Parker and Johnson, 2004). For the eastern two thirds of the United States, Schumacher and Johnson (2005, 2006) found that 66% of extreme rainfall events there are caused by quasi-linear MCSs, among which 54% are produced by only two modes in organization. The training line-adjoining stratiform (TL/AS) type often forms along (or north of) an east-west (E-W) aligned, pre-existing slow-moving surface boundary (such as a front or a convergence line), and a series of embedded "training" cells move eastward (also Stevenson and Schumacher, 2014; Peters and Roebber, 2014; Peters and Schumacher, 2015). The second type is quasi-stationary back-building (BB) systems, which depend more on meso- and storm-scale forcing and processes. In BB lines, new cells form repeatedly on the upstream side at nearly the same location then move downstream, making the line as a whole almost stationary (also Chappell, 1986; Corfidi et al., 1996). While some MCSs may possess characteristics of both types (Schumacher et al., 2011; Peters and Schumacher, 2015), the BB systems are typically smaller and more localized, and thus more difficult to predict (e.g., Schumacher and Johnson, 2005).

To repeatedly trigger new cells in BB MCSs at mid-latitudes, a well-known mechanism is through convectively-generated outflow boundary from downdrafts, i.e., at the leading edge

1   of the cold pool (or the gust front) that extends into the upwind side (e.g., Doswell et al., 1996;

2   Parker and Johnson, 2000; Corfidi, 2003; Schumacher and Johnson, 2005, 2009; Houston and

3   Wilhelmson, 2007; Moore et al., 2012), sometimes in conjunction with lifting along a frontal

4   boundary (e.g., Schumacher et al., 2011). Similar mechanisms for the BB process are also

5   found in some events in the East Asia (e.g., H. Wang et al., 2014; Jeong et al., 2015).

6   However, toward lower latitudes such as the subtropics and tropics, the environments may be

7   less conducive to cold pool development (e.g., Tompkins, 2001). Some studies on extreme

8   rainfall events in South China and Taiwan have shown that surface-based cold air produced

9   by previous convection that had dissipated for hours or even in the day before, when

10   impinged by the moist monsoonal flow, in particular the low-level jet (LLJ), can act to trigger

11   new convection in succession (e.g., Zhang and Zhang, 2012; Xu et al., 2012; C.-C. Wang et

12   al., 2014a; Luo et al., 2014). Such mechanisms by "cold domes," however, are different from

13   the lifting at gust fronts produced by coexisting, dissipating cells or those that had just

14   dissipated, and the induced MCSs may be less organized if a linear forcing such as a front or

15   low-level convergence zone is absent (e.g., Xu et al., 2012; C.-C. Wang et al., 2014b).

16   Many of the above heavy rainfall events in Taiwan occurred in the mei-yu season (May-June),

17   where repeated frontal passages affect the area during the transition period from northeasterly

18   to southwesterly monsoon (e.g., Ding, 1992; Chen, 2004; Ding and Chan, 2005). When the

19   mei-yu front approaches Taiwan, both the MCSs near the front or those associated with the

20   pre-frontal LLJ (south of the front) that impinges on the island can bring heavy rainfall (e.g.,

21   Chen and Yu, 1988; Kuo and Chen, 1990; Wang et al., 2005; C.-C. Wang et al., 2014a).

22   Under such conditions, BB MCSs may still develop (e.g., Li et al., 1997), in environments

23   that are not favorable for strong cold pools mainly due to high moisture content at low levels

24   (e.g., Tompkins, 2001; James and Markowski, 2010; Yu and Chen, 2011). For these systems,

25   the mechanism for upstream initiation of new cells at the end of the convective line,

26   presumably also dominated by storm-scale processes as their US counterparts (Schumacher

27   and Johnson, 2005), is not clear. Recently, the roles of pressure perturbation (p'), in particular

28   the dynamical pressure perturbation (p'_d, e.g., Rotunno and Klemp, 1982; Weisman and

29   Klemp, 1986; Klemp, 1987, and many others), in the evolution of convective cells inside the

30   E-W BB rainbands associated with Typhoon Morakot (2009) and extreme rainfall (e.g., Wang

31   et al., 2012) are examined by Wang et al. (2015, hereafter referred to as WKJ15). They found

32   that in the presence of an intense westerly LLJ, the interaction between updraft and vertical

33   wind shear (e.g., Klemp, 1987) induces positive (negative) p'_d at the western (eastern) flank

of the updraft below the jet-core level (with westerly shear) but a reversed pattern above (with easterly shear), and thus an upward-directed perturbation pressure gradient force (PGF) at the western (rear) flank (see e.g., Fig. 6 of WKJ15). This leads to a slow-down in the propagation speed of mature cells and promotes cell merger inside the rainbands, as often observed in quasi-linear multi-cell MCSs. A reduced speed of old cell and positive p'_d at its rear flank near the surface can also enhance convergence and contribute to upstream new cell initiation without the cold pool (WKJ15). Obviously, one question worth exploring is whether a mechanism similar to the Morakot case also plays an important role in other BB rainbands near Taiwan in the mei-yu season with the presence of a LLJ, or whether some other processes are also involved? Thus, we seek to further understand and clarify the details of the BB process in the case below.

During 11-12 June 2012, both TL/AS and BB MCSs developed in succession near northern Taiwan, and produced extreme rainfall up to 510 mm overnight (roughly during 14:00-24:00 UTC 11 June, where LST = UTC + 8 h), in Taipei City and the surrounding metropolitan area. Many densely-populated urban regions were flooded, and one day (12 June) was declared off work in Taipei, the first ever in Taiwan in mei-yu season due to heavy rainfall. Thus, this extreme-rainfall event was rare in its total amount, duration, and location. As will be shown later, clear BB behavior occurred in the quasi-stationary MCSs and contributed to the extreme rainfall in northern Taiwan in this event, among other factors linked to frontal forcing and topographic effects. Thus, this case is studied herein for details in the BB process at the convective scale, mainly through numerical simulation using a cloud-resolving model at a horizontal grid size of 1.5 km. Below, the data used and the methodology employed are described in Sect. 2, and the extreme rainfall event of 11-12 June 2012, including its synoptic environment, are overviewed in Sect. 3. In Sect. 4, our simulation results are validated against observations, and further used to investigate the formation mechanism of the linear MCS and the BB process upstream from the old cells. This evolution is then compared with the initiation of an isolated cell in Sect. 5 to identify the important factors in the BB process, and finally the conclusion and summary of this work are given in Sect. 6.

2 Data and methodology

2.1 Observational data

In this study, the data used include weather maps from the Central Weather Bureau (CWB) of Taiwan and gridded final analyses (0.5° × 0.5°, every 6 h) from the National Center for Environmental Prediction (NCEP) at 26 levels from 1000 to 10 hPa (including the surface level) covering the case period. The space-borne Advanced Scatterometer (ASCAT) observations are also used to assist the analysis of frontal position. For conditions in the pre-storm environment, the sounding at Panchiao (near Taipei City) is used. For the evolution of the MCS and the resulting rainfall, the vertical maximum indicator (VMI) composites of radar reflectivity and hourly data from the rain-gauge network (Hsu, 1998) in Taiwan, both provided by the CWB, are employed. The above observational data are used both for analysis and verification of model results.

2.2 The CReSS model and experiment

The Cloud-Resolving Storm Simulator (CReSS) is used for our numerical simulation. It is a cloud-resolving model that employs a nonhydrostatic and compressible equation set and a height-based terrain-following vertical coordinate (Tsuboki and Sakakibara, 2002, 2007). Clouds are treated explicitly in CReSS using a bulk cold-rain microphysical scheme (Lin et al., 1983; Cotton et al., 1986; Murakami, 1990; Ikawa and Saito, 1991; Murakami et al., 1994) with a total of six species (vapor, cloud water, cloud ice, rain, snow, and graupel). Sub-grid scale processes parameterized include turbulent mixing in the planetary boundary layer (PBL), radiation, and surface momentum and energy fluxes (Kondo, 1976; Louis et al., 1981; Segami et al., 1989). With a single domain (no nesting), this model has been used to study a number of heavy-rainfall events around Taiwan during the mei-yu season (e.g., C.-C. Wang et al., 2005, 2011, 2014a,b; Wang and Huang, 2009) as well as for real-time forecasts (e.g., Wang et al., 2013, 2016a; Wang, 2015, 2016). The CReSS model is open to the research community upon request, and its further details can be found in the works referenced above and at http://www.rain.hyarc.nagoya-u.ac.jp/~tsuboki/cress_html/index_cress_jpn.html.

In this study, the simulation is performed using a horizontal grid spacing of 1.5 km and a grid dimension (x, y, z) of 1000 × 800 × 50 points (cf. Fig. 1, Table 1). As already described, the NCEP 0.5° × 0.5° gridded final analyses serve as the initial and boundary conditions (IC/BCs)

5

1 of the model run from 12:00 UTC 10 June to 12:00 UTC 12 June 2012 (for 48 h). At the

2 lower boundary, real terrain at 30 s resolution (or $(1/120)°$, roughly 900 m) and observed

3 weekly sea surface temperature (SST, Reynolds et al., 2002) are provided. The model

4 configuration and major aspects of the experiment are summarized in Table 1.

2.3 Analysis of vertical momentum and pressure perturbations

6 To investigate the BB process taking place in the present case using model outputs, the

7 methods below, following Wilhelmson and Ogura (1972), Rotunno and Klemp (1982), Klemp

8 (1987), and Parker and Johnson (2004), are used to perform analysis of vertical momentum

9 and pressure perturbations. With the background environment assumed to be in hydrostatic

10 equilibrium, the vertical momentum equation can be written as

11
$$\frac{dw}{dt} = -\frac{1}{\rho}\frac{\partial p'}{\partial z} - \frac{\rho'}{\rho}g + F_z \approx -\frac{1}{\rho_0}\frac{\partial p'}{\partial z} - \frac{\rho'}{\rho_0}g + F_z \tag{1}$$

12 where all variables have their conventional meanings. Here, $\rho = \rho_0 + \rho'$, where ρ_0 is the

13 background value and ρ' the perturbation part of ρ, $B = -g(\rho'/\rho_0)$ is the buoyancy, and F_z is

14 the friction term by turbulent mixing. Thus, the vertical acceleration is driven by an imbalance

15 among the perturbation PGF, buoyancy, and turbulent mixing. The buoyancy is constituted by

16 the gaseous effect and the drag of all condensates, and can be expressed as

17
$$B = -\frac{\rho'}{\rho_0}g = g\frac{\theta'_v}{\theta_{v0}} - g\sum q_x \tag{2}$$

18 where θ_v is the virtual potential temperature (and $\theta_v = \theta_{v0} + \theta'_v$) and its perturbation accounts

19 for the gaseous effect, while q_x denotes the mixing ratio of any condensate species.

20 The perturbation pressure p' can be divided into the dynamical and buoyant components as p'

21 $= p'_d + p'_b$, and the diagnostic pressure equations for the anelastic set, with friction omitted

22 (e.g., Rotunno and Klemp, 1982; Parker and Johnson, 2004), are

23
$$\nabla^2 p'_b = \frac{\partial}{\partial z}(\rho_0 B) \text{ and} \tag{3}$$

24
$$\nabla^2 p'_d = -\rho_0\left[\left(\frac{\partial u}{\partial x}\right)^2 + \left(\frac{\partial v}{\partial y}\right)^2 + \left(\frac{\partial w}{\partial z}\right)^2 - w^2\frac{\partial^2}{\partial z^2}(\ln\rho_0)\right] - 2\rho_0(\frac{\partial v}{\partial x}\frac{\partial u}{\partial y} + \frac{\partial u}{\partial z}\frac{\partial w}{\partial x} + \frac{\partial v}{\partial z}\frac{\partial w}{\partial y}) \tag{4}$$

1   where ∇^2 is the laplacian operator. In both equations, a positive (negative) center in $\nabla^2 p'$

2   corresponds to a local minimum (maximum) in p' itself. Equation (3) states that p'_b is related

3   to the vertical gradient of the product of ρ_0 and B. On the RHS of Eq. (4), inside the brackets

4   are extension terms which imply maximized p'_d in regions of nonzero divergence or

5   deformation. The other terms inside the parentheses are shearing terms and imply minimized

6   p'_d in regions of nonzero vorticity (Parker and Johnson, 2004). The shearing effects include

7   those related to vertical wind shear ($\partial u/\partial z$ and $\partial v/\partial z$) associated with the LLJ, as reviewed in

8   Sect. 1 for the Morakot case. After $\nabla^2 p'_b$ or $\nabla^2 p'_d$ is obtained from Eqs. (3) or (4), the

9   relaxation method is used to solve the associated pressure perturbation through iteration (see

10   Appendix for details).

11   To provide additional verification, a second, independent method is also used in this study to

12   compute p' as in WKJ15. In this method, p' is separated from its background pressure (p_0),

13   defined as

14   $$p_0(x, y, z, t) = \langle p \rangle (x, y, z) + \Delta p(z, t),\tag{5}$$

15   where $\langle p \rangle$ is the time-averaged pressure over a fixed period, and Δp is the deviation of the

16   areal-mean pressure $\bar{p}$ at any given instant from its time mean $\langle \bar{p} \rangle$, such that

17   $$\Delta p(z, t) = \bar{p}(z, t) - \langle \bar{p} \rangle (z).\tag{6}$$

18   Thus, the gradual decrease of the areal-mean pressure with time as the mei-yu front

19   approaches from the north is reflected in Δp, and taken into account in p_0 besides the spatial

20   variation in mean (time-averaged) p [cf. Eq. (5)]. Then, p' is computed simply as

21   $$p'(x, y, z, t) = p(x, y, z, t) - p_0(x, y, z, t).\tag{7}$$

22   Referred to as the separation method, it is also applied to other variables to separate the

23   perturbation and the background where needed, such as for ρ and θ_v in Eqs. (1) and (2), as

24   well as potential temperature θ and horizontal wind components u and v.

25

3 Case overview

3.1 Synoptic and storm environment

In this section, the synoptic conditions and the BB rainbands responsible for the extreme rainfall are described. Figure 1 shows the surface weather map at 12:00 UTC 11 June 2012, about 2 h before heavy rainfall started in northern Taiwan. Extending from the East China Sea to southern China (ENE-WSW), the mei-yu front was about 130 km north of Taiwan, with almost an upright structure up to 700 hPa in the area. Based mainly on wind field since the mei-yu front near Taiwan is often associated with strong cyclonic shear vorticity but only weak thermal contrast (e.g., Kuo and Anthes, 1982; Chen et al., 2003; Wang et al., 2016b), the frontal position at this time in the NCEP 950-hPa analysis (Fig. 2a) is in agreement with the surface map, as is the ASCAT observation at 13:00 UTC (Fig. 2e). In the NCEP analysis, the strong southwesterly LLJ south of the front over the Taiwan Strait and off southeastern Taiwan is also revealed. While the LLJ reaches 20 m s^{-1} in maximum speed (at 950 hPa), the axis over the strait points toward northwestern Taiwan between the front and the island's topography (Fig. 2a). When the mei-yu front approaches and the prevailing southwesterly flow strengthens (mainly due to an increased pressure gradient), such a configuration is often produced in response to flow splitting due to terrain blocking and the subsequent channeling, confluence, and acceleration, with local wind maxima, i.e., barrier jets, near the two ends of Taiwan (e.g., Li and Chen, 1998; Wang ad Chen, 2002; Chen et al., 2005). For the one in northern Taiwan Strait (Fig. 2a), in particular, the low-level convergence (from confluence) associated with the barrier jet can provide the forcing for quasi-linear MCSs near or south of the front (e.g., Yeh and Chen, 2002; Wang et al., 2005). The NCEP analyses every 6 h shows that the 950-hPa front reached northern Taiwan near 00:00 UTC 12 June (Fig. 2c), also consistent with ASCAT data at 02:00 UTC (Fig. 2f). Afterward, as the rainfall in northern Taiwan gradually weakened (cf. Figs. 4 and 9, to be discussed later), the mei-yu front advanced rapidly across Taiwan and reached about 23°N within 6 h (Fig. 2c).

The Panchiao sounding (Fig. 3) in the Taipei metropolitan area (cf. Fig. 2c) at 12:00 UTC 11 June indicated very strong southwesterly flow throughout the lower troposphere, with a peak of 25 m s^{-1} near 925 hPa, consistent with the barrier jet in Fig. 2a (also e.g., Li and Chen, 1998; Chen et al., 2005). Near the surface, the temperature lapse rate was close to dry adiabats and indicated a well-mixed profile, while that further aloft was less steep but still mostly

exceeded the moist adiabats, indicating conditional instability up to about 550 hPa. The convective available potential energy (CAPE) was 583 J kg^{-1} and sufficient to support deep convection, if the air parcel could overcome the convective inhibition (CIN) of 78 J kg^{-1} to reach the level of free convection at 789 hPa. Obviously, these conditions were soon met since heavy rainfall did occur in Taipei. Note also that the humidity was quite high below about 550 hPa, and a dry layer did not exist throughout the troposphere. Thus, with instability and low-level convergence, the strong, deep, and moisture-laden southwesterly flow near and to the south of the approaching mei-yu front was clearly very favorable for active convection and substantial rainfall (e.g., Jou and Deng, 1992; C.-C. Wang et al., 2014a).

3.2 The back-building rainband with extreme rainfall

Figure 4 presents the composite VMI radar reflectivity from the ground-based radars in Taiwan at 1 h intervals, and depicts the evolution of the rainbands causing the extreme rainfall in northern Taiwan. At 12:00 UTC 11 June (Fig. 4a), an intense ENE-WSW-oriented squall line, with peak reflectivity in convective elements ≥50 dBZ, already formed and was approaching northern Taiwan to within about 30 km, i.e., at some 80-100 km ahead of the surface mei-yu front (cf. Figs. 1 and 2a). With a bulging middle section and trailing stratiform, the squall line moved southward at about 15 km h^{-1} and into northern Taiwan by 14:00 UTC (Fig. 4b and c). During the following hours through 18:00 UTC, this squall line continued to advance slowly and into 25°N, so that much of the northern Taiwan was covered by echoes with high reflectivity (Fig. 4d-g), while the stratiform region gradually moved eastward, in agreement with the upper-level wind (cf. Fig. 3). After 18:00 UTC, the convection through northern Taiwan evolved into a narrow line that remained quasi-stationary for hours until 23:00 UTC (Fig. 4g-l), with evident new development toward the west, i.e., back-building behavior (to be detailed later). Eventually, this linear MCS started to move south slowly and gradually away from the Taipei area after 00:00 UTC 12 June (Fig. 4m-o), likely in conjunction with the surface front with the arrival of the northeasterly flow (cf. Fig. 2c and f). During the entire period of Fig. 4, the mountain interiors in central and southern Taiwan also received continuous rainfall from forced uplift of the strong LLJ by the topography (cf. Fig. 2a and c), and another squall line also approached southern Taiwan from the west and made landfall near 22:00 UTC 11 June (Fig. 4i-o). Nonetheless, the reflectivity over northern Taiwan was both very active and lengthy, and produced by two types of MCSs: the first was

1 the squall line before 18:00 UTC 11 June and reminiscent to a TL/AS system, and the second

2 was the quasi-stationary BB MCS after 18:00 UTC (Fig. 4).

3 The distributions of 6 h accumulated rainfall during 12:00-18:00 and 18:00-24:00 UTC 11

4 June are shown in Fig. 5a and b. While three distinct rainfall centers over northern, central,

5 and southern Taiwan were produced in each period, the amount over northern Taiwan was the

6 highest. The rainfall during 12:00-18:00 UTC was maximized along the northwestern coast

7 and decreased inland (Fig. 5a), consistent with the MCS that moved in from the ocean (cf. Fig.

8 4). On the other hand, the rainfall was more concentrated during 18:00-24:00 UTC with

9 almost an E-W alignment, and the center was right near the Taipei City (Fig. 5b). The peak

10 amount during this later 6 h period was 311 mm, and an extreme value of 510 mm was

11 recorded overnight from the entire event. It is perhaps worthy to note that the mountainous

12 interior in central and southern Taiwan also received heavy rainfall since about 00:00 UTC 10

13 June (presumably due to forced uplift), but little rain fell over northern Taiwan prior to the

14 current event.

15 While back-building likely also occurred in the TL/AS-type squall line, such behaviors in the

16 quasi-stationary rainband after 18:00 were well depicted by the radar VMI reflectivity every

17 10 min (Fig. 6). As marked by the short arrows, frequent BB activities can be spotted at the

18 western end of the convective line or west of existing mature cells, and some of them were

19 quite close to the northwestern coast of Taiwan. After formation, they moved at small angles

20 from the ENE-WSW-oriented quasi-stationary line, repeatedly across northern Taiwan with

21 frequent cell mergers similar to those in WKJ15 (Fig. 6). The resulted rainfall in Fig. 5b, with

22 the maximum located inland near Taipei, also implies that many cells matured after they

23 moved onshore instead of over the ocean prior to landfall. Since the length of the line with

24 active cells upstream from Taipei is about 160 km and most cells travelled at the speed range

25 of 60-80 km h^{-1} in Fig. 6, the heavy rainfall would last only 2-2.5 h and much shorter than in

26 reality (cf. Fig. 5), if there were no new developments westward along the line.

27 In extreme events, there are often multiple factors of different scales working in synergy to

28 lead to their occurrence. This is also true in the present case, and the scenario leading to heavy

29 rainfall can be quite complicated. While the large and synoptic scale conditions provided a

30 favorable background (Figs. 1-3), the two MCSs developed south of the approaching mei-yu

31 front, in close proximity to the area of terrain-influenced low-level convergence (and the

32 barrier jet) near northern Taiwan (Figs. 2a, c, e, and f, and 4). In Figs. 4 and 6, the convective

lines even exhibited characteristics of multiple lines at times, possibly linked to gravity wave activities (e.g., Yang and Houze, 1995; Fovell et al., 2006). While the formation mechanism of the quasi-linear MCSs (the second one in specific) and the roles played by both the mei-yu front and the topography will be discussed and clarified (Sect. 4.2), the BB process at the convective scale was clearly also an important factor leading to the extreme rainfall, especially during the later 6 h period after 18:00 UTC (Fig. 6). Also, as typical in many events, the new BB cell is often found to develop about 15-30 km upstream from an old cell in Fig. 6. Thus, why this particular spot has an advantage for new cell initiation compared to other locations without a nearby old cell, is the scientific question that we wish to answer and the main focus of this case study. This specific question (and the formation mechanism of the MCSs) will be addressed through our numerical simulation results below.

4 Results of model simulation

4.1 Model result validation

As described in Sect. 2.2, our CReSS model simulation was performed from 12:00 UTC 10 June 2012 for 48 h using NCEP (0.5°) final analyses as IC/BCs, with a horizontal grid spacing of 1.5 km. The simulated winds and the front at an elevation of 549 m (close to 950 hPa) at 12:00 UTC 11 June (t = 24 h) and frontal positions every 6 h are shown in Fig. 2b and d. Compared to the observation and NCEP analyses (Figs. 1, 2a, and 2e), the simulated front in Fig. 2b is slightly too north, especially west of 120.5°E and over land in southeastern China, but the prefrontal LLJ is well captured, including the strong winds (barrier jet) near northern Taiwan. Linked to the position error of the front at 12:00 UTC, the modeled front is also too north at 18:00 UTC, but its western segment over the strait advanced southward more rapidly to catch up with the NCEP analyses during the next 6 h (Fig. 2c and d). The segment east of Taiwan, however, is still too north at 00:00 UTC 12 June (cf. Fig. 2f) and the position error there does not improve until about 12 h later (Fig. 2c and d).

The model-simulated surface winds at 10 m height and column-maximum mixing ratio of total precipitation every 2 h during 12:00-22:00 UTC 11 June are shown in Fig. 7, which can be compared with the radar composites in Fig. 4. In the model, the squall line before 18:00 UTC is along and to the north of the near-surface front (Fig. 7a-d) and different from the training-line system ahead of the front in the observation. Thus, the simulation of the first

1   MCS was not ideal in location, apparently linked to the frontal position error discussed earlier.

2   On the other hand, the quasi-stationary MCS over northern Taiwan since 18:00 UTC, with

3   intense convective cells near Taipei, as well as the second squall line over the southern strait,

4   are both nicely captured in the model as the front advanced south (Fig. 7d-f). As a result, the

5   rainfall simulation in northern Taiwan during 18:00-24:00 UTC, with a peak amount of 312

6   mm, is in close agreement with the observation (Fig. 5b and d), while that during the

7   preceding 6 h was not (Fig. 5a and c). Similar results are also revealed by hourly histogram of

8   rainfall in Fig. 8, averaged inside the elongated box depicted in Fig. 5b. The rainfall in

9   northern Taiwan was much better simulated in magnitude and variation in time after 18:00

10   UTC 11 June (Fig. 8), although the areal-averaged intensity in the model is somewhat lower

11   because the simulated rain belt is narrower than the one observed (Fig. 5b and d). Also, the

12   model predicted more rainfall than observed over the mountains in southern Taiwan than (Fig.

13   5), indicating that the flow over the terrain might be somewhat over-estimated, though this is

14   not our focus here.

15   **4.2 Formation of the quasi-linear MCS**

16   The more detailed distributions of horizontal winds and convergence/divergence near the

17   surface at 312 m from 18:30 to 21:00 UTC 11 June 2012 in the model are shown in Fig. 9.

18   With a wavy pattern and strong convergence along most of its length, the near-surface mei-yu

19   front (black dotted curves) is north of Taiwan but gradually approaches during this period.

20   Consistent with Figs. 1, 2, 6, and 7, the quasi-linear and stationary MCS, on the other hand,

21   developed south of the front near 25°N. As the front advances, their distance decreased from

22   about 90 km at 18:30 UTC to 30 km at 21:00 (Fig. 9), and in the observation the front only

23   caught up with the pre-frontal MCS after 00:00 UTC 12 June as mentioned (cf. Figs. 2c and

24   4g to o). Crossing northern Taiwan, the rainband forms along a near-surface convergence

25   zone (green dotted curves, mostly $> 5 \times 10^{-5}$ s^{-1} with confluence and acceleration) between

26   the flow blocked and deflected northward by the topography of Taiwan and the unblocked

27   flow farther to the north and west in the environment (but still ahead of the front, Fig. 9).

28   Thus, in agreement with the observations, the effects of terrain (blocking) played a major role

29   to initiate the rainband development, while the front helped provide and channel an enhanced

30   background flow with its approach in the present case. Such a scenario is quite similar to

31   those studied by Yeh and Chen (2002) and Wang et al., 2005).

1   Figure 10 shows the development and evolution of convective cells over northern Taiwan and

2   the upstream area in the model every 10 min during 19:20-22:10 UTC. In this quasi-stationary

3   system (cf. Figs. 7d-f and 9), the BB process is successfully simulated by CReSS. For

4   example, a new cell labeled as "A2" develops about 20 km upstream from the old cell "A1"

5   around 19:30 UTC, and becomes mature near 20:10 UTC. Likewise, "B2" is triggered west of

6   "B1" after 21:20 UTC, and develops into a mature cell near 21:40 UTC and then the two cells

7   merge near 21:50 UTC over northern Taiwan (Fig. 10, also cf. Fig. 9), in a way similar to that

8   discussed by WKJ15. In the model, the training of multiple cells in succession clearly leads to

9   heavy rainfall over the Taipei area (cf. Fig. 7e and f), in agreement with the observations.

10 Therefore, even though the simulation of the first TL/AS MCS is less than ideal, the model

11 results for the quasi-stationary BB lines (after about 18:00 UTC 11 June) can be used to

12 further investigate the BB process upstream from the old cells in this case. Thus, the area and

13 time period selected for the separation of p_0 and p', as described at the end of Sect. 2.3, are set

14 to 24.75-25.15°N, 120.35-121.75°E (cf. Fig. 7a) and over 18:00-24:00 UTC 11 June 2012.

15 **4.3   Structure of convective cells in the BB MCS**

16 In this subsection, the simulated structure of convective cells inside the BB system is first

17 examined, before the discussion on the finer details of pressure perturbations and their

18 associated effects in the BB process. The pair of old and new cells for study has been chosen

19 to be B1 and B2 over the period of 20:00-21:40 UTC, as they are farther away and less

20 affected by the terrain of northern Taiwan (cf. Fig. 10). To reveal the storm environment

21 (provided by the background forcing), E-W vertical cross-sections along 25°N through the

22 centers of both B1 and B2 (line AB in Fig. 10) are constructed and averaged over three

23 outputs from 21:25 to 21:35 UTC, as shown in Fig. 11a. The equivalent potential temperature

24 (θ_e) has a minimum of about 350 K at mid-levels (near 4-5 km) and increases both upward

25 and downward in upstream as well as downstream regions, indicating the presence of

26 convective (and conditional) instability (cf. Fig 3). During the average period, the mean

27 updraft of B1 is located near 121.35°E (cf. Fig. 10), and its immediate upstream region, i.e.,

28 where cell B2 is developing (~121.2°E), is characterized by strong near-surface convergence

29 coupled with upper-level divergence (Fig. 11a). Clearly favorable for new cell development

30 upstream with near-surface convergence there, such a thermodynamic and kinematic structure

31 under the influences of the front and terrain (as discussed in Sect. 4.2) is very similar to the

composites of BB MCSs in the USA obtained by Schumacher and Johnson (2005, their Fig. 17b). The WSW-ENE cross-section (along low-level flow) through B1 about 30 min earlier at 21:00 UTC shows a gradual acceleration of the upstream LLJ (thick arrow line) under the forcing of background convergence. As the jet approaches B1, which is already in mature stage (and quasi-steady), there is a rapid local acceleration then intense deceleration across B1, by about 10 m s^{-1} with a convergence in excess of 5×10^{-3} s^{-1} (Fig. 11b). While this local acceleration is clearly a response to the development of B1, the resulting vertical wind shear from the south-southwest is strongest below 500 m under B1 and its immediate upstream, where a value of about $2\text{-}3 \times 10^{-2}$ s^{-1} can be reached (Fig. 11c). The vertical wind shear upstream from B1 further aloft turns into northerly and then northeasterly at about 2 km, as expected above the axis of the LLJ, but its value ($\sim 3 \times 10^{-3}$ s^{-1}) is one order of magnitude smaller (Fig. 11c). Thus, the vertical wind shear in the storm environment of B1 (and B2) is strongest near the surface. Also, the deep convection can be seen to tilt eastward with height in both cross-sections, consistent with the direction of the upper-level winds and the evolution of stratiform area (cf. Figs. 3 and 4).

In Fig. 12, the perturbations in θ (i.e., θ') and horizontal winds (u' and v') obtained through the separation method (cf. Sect. 2.3), as well as the associated convergence and divergence, surrounding the pair of cells B1 and B2 at the surface between 20:00 and 21:00 UTC are presented every 20 min. During this initiation period of B2, while there exists positive θ' (of 0.4-0.8 K) below the updraft of B1, its induced cold pool is very weak at the surface, with a θ' of only -0.3 K at most, and is roughly 10 km to the east at the forward flank (Fig. 12). The convergence at the leading edge of the diverging, marginally colder air (denoted by dotted curves) extends to the southeast and south of B1 at 20:00-20:20 UTC (Fig. 12a and b), but gradually moves to the east afterwards (Fig. 12c and d). At the rear side of B1, the new cell B2 (marked by a blue "x") develops inside a region of surface convergence, consistent with Fig. 9d, e, and f, and quite far (at least 10 km) from both the weak cold pool and the leading edge of its outflow (Fig. 12). Therefore, the cold pool does not play any significant role in the initiation of the back-building cell B2 in the model, and the B1-B2 pair appears to be ideal for further investigation in greater detail.

The results of $\nabla^2 p'$ obtained by the two different methods (by separation and from Eqs. 3 and 4) as described in Sect. 2.3 at two different heights near 0.8 and 3 km are compared in Fig. 13, also for 21:00 UTC as an example. In general, the patterns are very similar. At 0.8 km,

1   negative $\nabla^2 p'$ (implying $p' > 0$) occurs near the updraft of B1 with positive $\nabla^2 p'$ (implying p'

2   < 0) to the east near the downdraft (Fig. 13a and b). West of B1 where B2 is developing,

3   positive (negative) $\nabla^2 p'$ is found to the south (north) of the near-surface convergence zone.

4   Near 3 km, the updraft of B1 corresponds to $\nabla^2 p' > 0$ and $\nabla^2 p' < 0$ occurs to its western flank

5   and further upstream over B2 (Fig. 13d and e). The laplacian of buoyancy pressure

6   perturbation ($\nabla^2 p'_b$) alone computed from Eq. (3) closely resembles that of the total pressure

7   perturbations at both levels (except perhaps a slight southward shift near the updraft of B1 at

8   0.8 km), implying a dominant role of p'_b over p'_d in this event. Nevertheless, Fig. 13 confirms

9   that the two methods yield consistent results.

10 ### 4.4   Analysis of pressure perturbations

11   To examine the distributions of pressure perturbations and their roles in the BB process in

12   greater detail, a series of vertical cross-sections through the updraft center of B1 at 5 km and

13   the near-surface center of B2 from 20:00 to 21:00 UTC (each roughly 50 km in length, cf.

14   Figs. 10 and 12), i.e., during the initiation stage of B2, are constructed. Here, the structures of

15     $\nabla^2 p'$ are first presented, so as to better infer to the patterns of p' discussed later through Eqs.

16   (3) and (4). At 20:00 UTC when signs of B2 are yet to appear (Fig. 14a), the updraft of B1

17   (>5 m s^{-1}) is more upright with downdrafts at both flanks (>1 m s^{-1} at mid-level or above). At

18   the backside (upstream) of the updraft, in particular, $\nabla^2 p'$ is positive at mid-level and negative

19   both above and below, corresponding to $p' < 0$ and $p' > 0$, respectively (as labeled by "L" and

20   "H"). Again, the pattern of $\nabla^2 p'$ is largely attributable to its buoyant ($\nabla^2 p'_b$) instead of

21   dynamical component ($\nabla^2 p'_d$, Fig. 14b and c). Twenty minutes later at 20:20 UTC (Fig. 14d),

22   the updraft of B1 strengthens to more than 8 m s^{-1} and becomes more tilted, but the basic

23   pattern of $\nabla^2 p'$ at its western flank and the upstream region remains. At this time, the

24   suppressing downdraft there weakens, and B2 is developing (~ 0.5 m s^{-1}) just west of the

25   sinking motion and about 15 km upstream from the core of B1. This new development is

26   associated with $p' < 0$ below 1 km and $p' > 0$ over 1-3 km, and the perturbations (and those of

27   B1) are also mainly from the buoyant rather than dynamical effects (Fig. 14e and f).

28   At 20:40 UTC (Fig. 14g), B1 further strengthens and is even more tilted with height, and its

29   associated downdraft below the mid-level (> 2 m s^{-1} near 4 km) now appears only at the

30   eastern (downwind) side (cf. Fig. 12c). The upward motion of B2 can now reach over 1 m s^{-1}

31   and extend further upstream, while a layer of positive $\nabla^2 p'$ (implying $p' < 0$) forms near 5 km,

1 again mainly from the buoyant effects (cf. Fig. 14h). The distribution of $\nabla^2 p'_d$ is only

2 significant at both flanks of the updraft of B1 below about 3.5 km (and at its eastern flank

3 near 5 km, Fig. 14i), which forms gradually as B1 intensifies (Fig. 14c and f). The

4 configuration of positive (negative) p'_d at the rear (forward) flank of the updraft near 500 mm

5 (below the jet level, cf. Fig. 11c) and a reversed pattern above (near 2-3 km) is consistent with

6 the shearing (plus extension) effect (cf. Eq. 4), in agreement with WKJ15 and other earlier

7 studies. However, since w and its horizontal gradient are weak near the surface, where the

8 vertical wind shear is larger (also Fig. 11c), the value of $\nabla^2 p'_d$ is smaller than that in WKJ15.

9 Also, due to the farther distance, a direct role played by the dynamical pressure perturbations

10 in new cell initiation of B2 appears limited in the present case here.

11 Both B1 and B2 intensify at 21:00 UTC, and the latter, peaking at about 1.5 m s^{-1}, can now

12 reach 4 km while the layer of $\nabla^2 p' > 0$ above (near 5 km) also grows stronger (Fig. 14j). A

13 downdraft at the rear flank of B1 reappears at mid-levels and penetrates down to 3 km at this

14 time, and acts to separate B2 from B1 (also Fig. 13d). Like earlier times since 20:20 UTC, the

15 total pattern of $\nabla^2 p$ is dominated by $\nabla^2 p'_b$ everywhere, except near the based of B1 (below

16 1.5 km) where $\nabla^2 p'_d$ contributes significantly (Fig. 14k and l). Thus, the buoyancy-related

17 effect is consistently the more dominant one in the region of B2 during its initiation stage in

18 the model, suggesting the importance of near-surface convergence in driving the development

19 of the line-shaped MCS in this event, as also shown earlier in Sect. 4.2 (and cf. Fig. 11a).

20 Nevertheless, the propagation speed of B1 is indeed slower than B2 in Fig. 10, and can be

21 estimated to be about 8.9 m s^{-1} near 21:00 UTC. Caused by the dynamical effect of p'_d, this

22 slow down implies an increase in low-level blocking, and subsequent upstream convergence

23 by about 1×10^{-4} s^{-1} using Fig. 11b (with a LLJ of 12.5 m s^{-1} near 40 km upstream), or 2.2 $\times$

24 10^{-4} s^{-1} larger than its surrounding with a background speed divergence of ~1.2×10^{-4} s^{-1}

25 following WKJ15 (p.11109). Since this is no more than 20% of the maximum convergence

26 near B2 and its immediate upstream (west of 121.2°E, cf. Fig. 11a), the minor role of p'_d in

27 the initiation of B2 in the present case can be confirmed.

28 The buoyancy B (or more precisely, the vertical buoyant force per unit mass) in Eq. (1) and its

29 contributing terms as given in Eq. (2) on the same vertical cross-sections are shown in Fig. 15.

30 At 20:00 UTC, as expected, B is positive inside the cumulonimbus B1, and negative in the top

31 portion of the cloud (> 6.5 km) and below the main updraft (< 2 km, Fig. 15a). Such a pattern

1   is due to the combined effects of positive virtual potential temperature perturbation ($\theta'_v > 0$)

2   clearly from latent heat release (LHR) inside the cloud, and the downward drag by all

3   hydrometeors (including both cloud particles and precipitation) maximized below the updraft

4   core (Fig. 15b and c). In the downdrafts at the flanks (which originate from higher levels), B

5   and $g(\theta'_v/\theta_{v0})$ are also mostly positive from adiabatic warming outside the cloud.

6   From 20:20 to 21:00 UTC when the updraft of B1 becomes increasingly tilted, the buoyancy

7   B in the core region of the updraft remains positive because of LHR, as the drag force shifts

8   toward the downwind side (Fig. 15d-l). Below and east of the updraft, B is strongly negative

9   near the surface due to the drag and a rapid reduction in positive θ'_v as the air descends. Even

10   though this reduction in θ'_v suggests some evaporative cooling, the cold pool (and surface

11   outflow) would be to the east of B1, as confirmed in Fig. 12. On the upstream side where B2

12   is developing, $B > 0$ appears near the surface with $B < 0$ further aloft at 2-5 km (Fig. 15d, g,

13   and j) and can be attributed, respectively, to LHR and adiabatic cooling associated with

14   ascending motion (Fig. 15e, h, and k) in a convectively unstable environment. Apparently, as

15   B2 develops, the cooling above it and to the west (roughly 120.8-121°E) leads to a layer of

16   positive $\partial B/\partial z$ and $\nabla^2 p'_b$ near 5 km (cf. Eq. 3), since the air further above is stable (cf. Fig.

17   11a). In Fig. 15, however, one particular center of negative B, near 120.85°E and 3 km at

18   20:20 UTC, develops in a sinking area at the western edge of the cumulus, and therefore is

19   also enhanced by evaporative cooling of cloud droplets (Fig. 15d-l). Thus, the cooling and

20   subsequently $B < 0$ (near 3 km) associated with B2 is not only by the adiabatic effect, but also

21   by evaporation at an earlier stage of initiation, for example, around 20:20 UTC (Fig. 15d and

22   e). However, at later times when the updraft of B1 becomes more tilted and B2 grows higher

23   and stronger, it becomes more difficult for the rear-flank downdraft to reach close to the

24   surface (cf. Fig. 15j-l), even though its strength can be sensitive to the cloud microphysical

25   scheme (e.g., Morrison et al., 2009).

26   Upstream from B1, the near-surface warming and cooling above, with maxima near 1 km and

27   3-4 km, respectively, create a decrease in buoyancy with height ($\partial B/\partial z < 0$) that grows

28   stronger with time near B2 (Fig. 15d, g, and j). Together with the (near) exponential decrease

29   of ρ_0 upward, this condition leads to $\nabla^2 p'_b < 0$ in Eq. (3), and thus $p'_b > 0$ that peaks slightly

30   above 1 km and intensifies through time, as obtained using the relaxation method (Sect. 2.3)

31   and shown in Fig. 16 (middle column). The upward decrease of p'_b, as the major component

32   of total p', in turn produces an upward-directed buoyant PGF to help B2 develop further (Fig.

16, left and middle columns). Thus, the combined effect of buoyancy B (cf. Fig. 15, left column) and total perturbation PGF in the vertical [cf. Eq. (1)] is upward acceleration of parcels in B2 (Fig. 16, right column) to eventually reach free ascent and ignite deep convection (near 21:20 UTC, cf. Fig. 10).

5   Discussion

In the previous section, the pressure perturbation and buoyancy, dominated by the thermodynamic effects (including both adiabatic and diabatic ones from condensation or evaporation), as well as the resultant upward development at the initiation stage of cell B2 are examined (Figs. 13-16). The specific roles played by the old cell B1 in triggering B2, however, are still not fully clear. Therefore, we further compare the initiation of an isolated cell farther upstream, C1, where no existing cell is present nearby (cf. Figs. 9f and 10), with B1-B2 pair and discuss their differences. Obviously, cells like C1 can also develop on its own under the background forcing (cf. Fig. 9), as also seen in Fig. 6, but a comparison allows us to identify the additional role of B1 to new cell triggering, and thus to the BB process about 15-30 km upstream of the old cell in the present case.

Figure 17 shows similar plots as in Fig. 14, but through cell C1 on cross sections along the low-level convergence zone (WSW-ENE oriented) at 20:40 and 21:20 UTC, at the beginning of the initiation and right before the break out of deep convection, respectively (cf. Fig. 10). At 20:40 UTC (Fig. 17a), C1 is located near the left edge of the plots, while B2 appears near the right edge. At this early stage, the weak rising motion is associated with $\nabla^2 p' > 0$ (or $p' < 0$) below about 1 km and $\nabla^2 p' < 0$ (or $p' > 0$) slightly above near 1-2.5 km, again mostly from the buoyant component (Fig. 17a-c). This pattern is because B is maximized near 1 km even though its value is negative ($B < 0$) everywhere (not shown), indicating that the near-surface atmosphere is still stable and the positive w is forced by the convergence at this time.

At 21:20 UTC when C1 grows much stronger ($\sim$1.5 m s^{-1}), the same pattern continues to amplify and extends upward, while p'_d remains to play little role without a mature cell (Fig. 17d-f). Now, with clouds reaching about 5 km, B has become positive at the core of C1 (peaking over 2×10^{-3} m s^{-2} near 1.5 km) due to LHR after saturation (Fig. 18a and b), giving a largest θ'_v of $\sim$1.2 K (not shown). Near the cloud top and below the cloud base of C1, both B and θ'_v turn negative and can only come from adiabatic or evaporative cooling, or both. The

1 cooling near 5-6 km explains the layer of $\nabla^2 p'_b$ (and $\nabla^2 p'$) > 0 immediately above (over 6-7

2 km, Fig. 17d and e), as seen earlier in Fig. 14g and 14j above the developing B2 (near 5 km).

3 The solutions of p' and p'_b by the relaxation method, linked to the pattern of their laplacian

4 noted above, produce downward perturbation PGF (below ~2 km, Fig. 18c and d) that

5 partially cancels the upward buoyant force (cf. Fig. 18a).

6 Overall, the warming by LHR and the cooling above during the developing stage of new cells

7 represent a destabilization in their low-level environment with time (Figs. 15 and 18). Forced

8 by the background convergence (cf. Fig. 9), even though C1 eventually also develops into

9 deep convection, the vertical perturbation PGF remains pointing down below about 2.5 km

10 even at 21:20 UTC (Fig. 18c and d). On the contrary, it is positive above 1-1.5 km in B2 and

11 helps its development at both 20:40 and 21:00 UTC (Fig. 16d and g). Consistent with this

12 difference, in B2, the maximum center of p'_b occurs closer to the surface and it decreases with

13 height more rapidly above, and three factors linked to the old cell B1 contribute to the

14 establishment of the upward-directed perturbation PGF. First, a stronger cooling occurs near 3

15 km above B2 (Fig. 15), at levels significantly lower than that above C1 (cf. Fig. 18), and this

16 cooling is likely enhanced by evaporation of condensates near the western edge of B1

17 (besides adiabatic effect). Second, a more rapid and efficient warming also occurs closer to

18 the surface at the early stage of B2, and this is helped by the stronger LHR near the bottom of

19 B1 (cf. Fig. 15). Both these effects can be thought of as a more rapid destabilization that gives

20 the new cell the potential for a faster development. Finally, the separation by the descending

21 branch of the old cell, when such a descent can reach a lower elevation, also plays a role in

22 leading to BB process about 20 km upstream in the present case, based on our numerical

23 simulation results in this case study. In C1 where $B > 0$ is counteracted by a downward

24 perturbation PGF, all three advantages are absent without a nearby old cell (Figs. 17 and 18).

6   Conclusion and summary

27 During 11-12 June 2012 in the mei-yu season, both TL/AS and BB MCSs developed in

28 succession near northern Taiwan, and together produced extreme rainfall up to 510 mm

29 overnight in the Taipei metropolitan area, causing serious flooding in many densely-populated

30 regions. Observations show that BB behavior occurred in these MCSs, especially in the

31 second, E-W-aligned quasi-stationary linear MCS during 18:00-24:00 UTC 11 June (02:00-

32 08:00 LST 12 June), and was a contributing factor to the extreme rainfall and related hazards

1 in Taipei. The numerical simulation using the CReSS model with a horizontal grid size of 1.5

2 km starting at 12:00 UTC 10 June successfully captured the development and evolution of the

3 BB MCS (but with considerable position error for the preceding TL/AS system). In contrast

4 to mid-latitude (and some subtropical) systems, the cold pool mechanism is not responsible

5 for triggering new BB cells in the present MCS, and thus the model results are used to

6 investigate the details of the BB process occurring specifically about 15-30 km upstream from

7 old convective elements in this subtropical system.

8 In agreement with and supported by the observations, the linear BB MCS in the present event

9 was forced by near-surface convergence ahead of the front, between the flow blocked and

10 deflected northward (into southwesterly) by the topography of Taiwan and the unblocked

11 (west-southwesterly) flow farther to the north and west in the environment. The approaching

12 mei-yu front (about 80-30 km) to the north of the linear MCS, thus, helped provide and

13 channel an enhanced prevailing flow to its south but did not play a direct role in the formation

14 of the MCS.

15 For the BB process at the convective scale, although the dynamic pressure perturbations (p'_d)

16 from the interaction between the mature cells and the LLJ, with $p'_d > 0$ (< 0) at the rear

17 (forward) flank of the updraft near the surface below the jet and a reversed pattern near 2-3

18 km above the jet, can cause the mature cells to slow-down slightly and enhance the low-level

19 convergence upstream, their effects are weaker compared to those found in WKJ15 for a case

20 of typhoon rainband, and a direct role in new cell initiation appears quite limited.

21 In the present event, the total pressure perturbations (p') in the vicinity of the new cell

22 throughout the initiation stage are attributed more to their buoyant (p'_b) than dynamical

23 component. Forced by the low-level convergence (parallel to the line) in the background, the

24 early development of new cells, at convective scale, are associated with positive buoyancy (B

25 > 0) by latent heating below and negative buoyancy ($B < 0$) by adiabatic cooling above, and

26 this represents a gradual destabilization in their surrounding environment. By comparing the

27 BB process with the initiation of an isolated cell, the additional and specific roles played by

28 the old cell to help trigger new convection to its west can be identified. At the initial stage, the

29 development is close to the mature cell, which provides stronger warming below (and closer

30 to the surface) and also additional cooling above from evaporation of condensates at its rear

31 side. The more rapid upward decrease in B produces a positive p'_b at a lower height and

32 subsequently an upward-directed perturbation (buoyant) PGF that drives further development

1 together with the positive buoyancy. Thus, the net effect of the additional warming/cooling is

2 essentially a more rapid destabilization that gives the new cell a faster development. After

3 some time when the new cell has gain sufficient strength, a descending branch appearing at

4 the rear flank of the old cell acts to separate the new cell to about 20 km upstream. The new

5 cell continues to strengthen there, and eventually deep convection is ignited. Thus, the above

6 roles played by the existing old cells, largely thermodynamic in origin but also helped by

7 dynamical and kinematic effects, can explain why the spot roughly 15-30 km upstream from

8 the western end of quasi-linear MCSs in the subtropics can often have advantages over other

9 locations for new cell initiation in their back-building process, even in the absence of cold

10 pool mechanism. To our knowledge, the above favorable factors that can be provided by the

11 old cells in the BB MCSs, particularly not in association with the cold pool, have not been

12 investigated in the literature before.

13

14 Acknowledgements

20

21 Appendix   The relaxation method

22 In this study, the relaxation method is used to numerically solve for the pressure perturbation

23 p from its 3-D laplacian $\nabla^2 p$ ("prime" omitted for simplicity), where $\nabla^2 p$ can be $\nabla^2 p_b$, $\nabla^2 p_d$,

24 or any of the rhs terms in Eq. (3) or (4). In this appendix, its formulation and boundary

25 conditions are described. Since the vertical grid spacing of CReSS is stretched, the values of

26 $\nabla^2 p$ (and all other known variables in need) are first vertically interpolated to grid with a fixed

27 Δz of 100 m, such that $\Delta x = \Delta y = 1$ km $= 10 \, \Delta z$. At second-order accuracy, the 3-D laplacian

28 inside the calculation domain is approximated by the central-difference method as

29 $$\nabla^2 p = \frac{p_{x+1} + p_{x-1} - 2p}{\Delta x^2} + \frac{p_{y+1} + p_{y-1} - 2p}{\Delta y^2} + \frac{p_{z+1} + p_{z-1} - 2p}{\Delta z^2} \qquad \text{(A1)}$$

1 where subscripts represent the p values of the next grid point on either side in each direction.

2 After rearranging terms to move only p (unknown) on the lhs and using $\Delta x = \Delta y = 10\,\Delta z$, Eq.

3 (A1) can be rewritten as

4 $$p = \frac{p_{x+1} + p_{x-1} + p_{y+1} + p_{y-1} + 10^2(p_{z+1} + p_{z-1}) - (\Delta x^2 \cdot \nabla^2 p)}{4 + 2 \times 10^2} \tag{A2}$$

5 and used for interior grid points. On the boundary of the domain, the Neumann condition is

6 applied and the next grid point outside is assumed to have the same value as the one on the

7 boundary. For example, $p_{x-1} = p$ on the western boundary, and the laplacian in x-direction

8 ($\nabla^2 p_x$) in (A1) reduces to

9 $$\nabla^2 p_x = \frac{p_{x+1} - p}{\Delta x^2} \tag{A3}$$

10 while the two other rhs terms in y and z directions remain unchanged. So, on the western

11 boundary, the p_{x-1} term vanishes and the formula equivalent to Eq. (A2) becomes

12 $$p = \frac{p_{x+1} + p_{y+1} + p_{y-1} + 10^2(p_{z+1} + p_{z-1}) - (\Delta x^2 \cdot \nabla^2 p)}{3 + 2 \times 10^2}. \tag{A4}$$

13 Thus, on each of the remaining sides (and edges and corners) along the boundary of the 3-D

14 domain, the formula would take a different form from (A2) following a similar derivation.

15 Since the procedures are quite straight-forward, they are not repeated here.

16 Using equations including (A2) and (A4), the values of p can be numerically solved through

17 iteration. Starting from a set of first guess of p, all the terms on the RHS are known or can be

18 computed, and a new set of p on the LHS is obtained in each iteration going through all the

19 grid points. After each iteration, Eq. (A1) (or its equivalents on the boundaries) is used to

20 compute $\nabla^2 p$ from the newly-obtained p and check against the true value (from Eqs. 3 or 4).

21 When the total absolute error of $\nabla^2 p$ summed over all grid points reduces below the specified

22 threshold, the result converges and the iteration stops. Figures 13 and 15 of WKJ15 provide

23 some examples of the results obtained using the same relaxation method.

24

References

Bluestein, H. B., and Jain, M. H.: Formation of mesoscale lines of precipitation: severe squall lines in Oklahoma during the spring, J. Atmos. Sci., 42, 1711-1732, 1985.

Brooks, H. E., and Stensrud, D. J.: Climatology of heavy rain events in the United States from hourly precipitation observations, Mon. Weather Rev., 128, 1194-1201, 2000.

Browning, K. A.: Organization of clouds and precipitation in extratropical cyclones, in: Extratropical Cyclones: The Erik Palmén Memorial Volume, edited by: Newton, C. W. and Holopanien, E. O., Am. Meteor. Soc., Boston, MA, USA, 129-153, 1990.

Carbone, R. E.: A severe frontal rainband. Part I: Stormwide hydrodynamic structure, J. Atmos. Sci., 39, 258-279, 1982.

Chappell, C. F.: Quasi-stationary convective events, in: Mesoscale Meteorology and Forecasting, edited by: Ray, P., Am. Meteor. Soc., Boston, MA, USA, 289-310, 1986.

Chen, G. T.-J.: Research on the phenomena of Meiyu during the past quarter century: An overview, World Scientific Series for Meteorology of East Asia Volume 2. East Asian Monsoon, edited by: Chang, C.-P. #et al., 357-403, 2004.

Chen, G. T.-J., and Chou, H.-C.: General characteristics of squall lines observed in TAMEX, Mon. Weather Rev., 121, 726-733, 1993.

Chen, G. T.-J., and Yu, C.-C.: Study of low-level jet and extremely heavy rainfall over northern Taiwan in the mei-yu season. Mon. Weather Rev., 116, 884-891, 1988.

Chen, G. T.-J., Wang, C.-C., and Liu, S. C.-S.: Potential vorticity diagnostics of a Mei-yu front case. Mon. Weather Rev., 131, 2680-2696, 2003.

Chen, G. T.-J., Wang, C.-C., and Lin, D. T.-W.: Characteristics of low-level jets over northern Taiwan in Mei-yu season and their relationship to heavy rain events, Mon. Weather Rev., 133, 20-43, 2005.

Corfidi, S. F.: Cold pools and MCS propagation: forecasting the motion of downwind-developing MCSs, Weather Forecast., 18, 997-1017, 2003.

Corfidi, S. F., Meritt, J. H., and Fritsch, J. M.: Predicting the movement of mesoscale convective complexes, Weather Forecast., 11, 41-46, 1996.

1 Cotton, W. R., Tripoli, G. J., Rauber, R. M., and Mulvihill, E. A.: Numerical simulation of the
2   effects of varying ice crystal nucleation rates and aggregation processes on orographic
3   snowfall, J. Clim. Appl. Meteorol., 25, 1658-1680, 1986.

4 Ding, Y.: Summer monsoon rainfalls in China. J. Meteor. Soc. Jpn., 70, 373-396, 1992.

5 Ding, Y., and Chan, J. C.-L. Chan: The East Asian summer monsoon: An overview. Meteor.
6   Atmos. Phys., 89, 117-142, 2005.

7 Doswell, C. A., III: Severe convective storms – an overview, in: Severe Convective Storms,
8   Meteor. Monogr., No. 50, Am. Meteor. Soc., Boston, MA, USA, ISBN: 978-1-878220-41-
9   7, 1-26, 2001.

10 Doswell, C. A., III, Brooks, H. E., and Maddox, R. A.: Flash flood forecasting: an
11   ingredients-based methodology, Weather Forecast., 11, 560-581, 1996.

12 Fovell, R. G., Mullendore, G. L., and Kim, S.-H.: Discrete propagation in numerically
13   simulated nocturnal squall lines, Mon. Weather Rev., 134, 3735-3752, 2006.

14 Houston, A. L., and Wilhelmson, R. B.: Observational analysis of the 27 May 1997 central
15   Texas tornadic event. Part I: Prestorm environment and storm maintenance/propagation,
16   Mon. Weather Rev., 135, 701-726, 2007.

17 Houze, R. A., Jr., Smull, B. F., and Dodge, P.: Mesoscale organization of springtime
18   rainstorms in Oklahoma, Mon. Weather. Rev., 118, 613-654, 1990.

19 Hsu, J.: ARMTS up and running in Taiwan, Väisälä News, 146, 24-26, 1998.

20 Ikawa, M., and Saito, K.: Description of a nonhydrostatic model developed at the Forecast
21   Research Department of the MRI, MRI Tech. Rep. 28, Tsukuba, Japan, 238 pp, 1991.

22 James, R. P., and Markowski, P. M.: A numerical investigation of the effects of dry air aloft
23   on deep convection, Mon. Weather Rev., 138, 140-161, 2010.

24 Jeong, J.-H., Lee, D.-I., and Wang, C.-C.: A study on an extreme rainfall-producing quasi-
25   stationary mesoscale convective system over southeastern Korea. Impact of cold pool,
26   Mon. Weather Rev., revised, 2016.

27 Johnson, R. H., and Mapes, B. E.: Mesoscale processes and severe convective weather, in:
28   Severe Convective Storms, edited by: Doswell, C. A., III, Meteor. Monogr., No. 50, Am.
29   Meteor. Soc., Boston, MA, USA, ISBN: 978-1-878220-41-7, 71-122, 2001.

Jou, B. J.-D., and Deng, S.-M.: Structure of a low-level jet and its role in triggering and organizing moist convection over Taiwan: A TAMEX case study. Terr. Atmos. Oceanic Sci., 3, 39-58, 1992.

Klemp, J. B.: Dynamics of tornadic thunderstorms, Annu. Rev. Fluid Mech., 19, 369-402, 1987.

Kondo, J.: Heat balance of the China Sea during the air mass transformation experiment, J. Meteor. Soc. Jpn., 54, 382-398, 1976.

Kuo, Y.-H., and Anthes, R. A.: Numerical simulation of a Mei-Yu system over southeastern Asia. Pap. Meteor. Res., 5, 15-36, 1982.

Kuo, Y.-H., and Chen, G. T.-J.: The Taiwan Area Mesoscale Experiment (TAMEX): An overview. Bull. Amer. Meteor. Soc., 71, 488-503, 1990.

LeMone, M. A., Zipser, E. J., and Trier, S. B.: The role of environmental shear and thermodynamic conditions in determining the structure and evolution of mesoscale convective systems during TOGA COARE, J. Atmos. Sci., 55, 3493-3518, 1998.

Li, J., and Chen, Y.-L.: Barrier jets during TAMEX, Mon. Weather Rev., 126, 959-971, 1998.

Li, J., Chen, Y.-L., and Lee, W.-C.: Analysis of a heavy rainfall event during TAMEX, Mon. Weather Rev., 125, 1060-1082, 1997.

Lin, Y.-L., Farley, R. D., and Orville, H. D.: Bulk parameterization of the snow field in a cloud model, J. Clim. Appl. Meteorol., 22, 1065-1092, 1983.

Louis, J. F., Tiedtke, M., and Geleyn, J. F.: A short history of the operational PBL – parameterization at ECMWF, in: Proceedings, ECMWF Workshop on Planetary Boundary Layer Parameterization, Reading, UK, 59-79, 1981.

Luo, Y., Gong, Y., and Zhang, D.-L.: Initiation and organizational modes of an extreme-rain-producing mesoscale convective system along a Mei-yu front in East China, Mon. Weather Rev., 142, 203-221, 2014.

Morrison, H., Thompson, G., and Tatarskii, V.: Impact of cloud microphysics on the development of trailing stratiform precipitation in a simulated squall line: Comparison of one- and two-moment schemes, Mon. Weather Rev., 137, 991-1007, 2009.

1   Maddox, R. A., Chappell, C. F., and Hoxit, L. R.: Synoptic and meso-α scale aspects of flash
2   flood events, Bull. Am. Meteor. Soc., 60, 115-123, 1979.

3   Meng, Z., Yan, D., and Zhang, Y.: General features of squall lines in East China, Mon.
4   Weather Rev., 141, 1629-1647, 2013.

5   Moore, B. J., Neiman, P. J., Ralph, F. M., and Barthold, F. E.: Physical processes associated
6   with heavy flooding rainfall in Nashville, Tennessee, and vicinity during 1-2 May 2010:
7   The role of an atmospheric river and mesoscale convective systems, Mon. Weather Rev.,
8   140, 358-378, 2012.

9   Murakami, M.: Numerical modeling of dynamical and microphysical evolution of an isolated
10   convective cloud---The 19 July 1981 CCOPE cloud, J. Meteor. Soc. Jpn., 68, 107-128,
11   1990.

12 Murakami, M., Clark, T. L., and Hall, W. D.: Numerical simulations of convective snow
13   clouds over the Sea of Japan: two-dimensional simulation of mixed layer development and
14   convective snow cloud formation, J. Meteor. Soc. Jpn., 72, 43-62, 1994.

15 Parker, M. D., and Johnson, R. H.: Organizational modes of midlatitude mesoscale convective
16   systems, Mon. Weather Rev., 128, 3413-3436, 2000.

17 Parker, M. D., and Johnson, R. H.: Structures and dynamics of quasi-2D mesoscale
18   convective systems, J. Atmos. Sci., 61, 545-567, 2004.

19 Peters, J. M., and Roebber, P. J.: Synoptic control of heavy-rain-producing convective
20   training episodes, Mon. Weather Rev., 142, 2464-2482, 2014.

21 Peters, J. M., and Schumacher, R. S.: Mechanisms for organization and echo training in a
22   flash-flood-producing mesoscale convective system, Mon. Weather Rev., 143, 1058-1085,
23   2015.

24 Rotunno, R., and Klemp, J. B.: The influence of the shear-induced pressure gradient on
25   thunderstorm motion, Mon. Weather Rev., 110, 136-151, 1982.

26 Rotunno, R., Klemp, J. B., and Weisman, M. L.: A theory for strong, long-lived squall lines, J.
27   Atmos. Sci., 45, 463-485, 1988.

28 Schumacher, R. S., and Johnson, R. H.: Organization and environmental properties of
29   extreme-rain-producing mesoscale convective systems, Mon. Weather Rev., 133, 961-976,
30   2005.

Schumacher, R. S., and Johnson, R. H.: Characteristics of U.S. extreme rain events during 1999-2003, Weather Forecast., 21, 69-85, 2006.

Schumacher, R. S., and Johnson, R. H.: Quasi-stationary, extreme-rain-producing convective systems associated with midlevel cyclonic circulations, Weather Forecast., 24, 555-574, 2009.

Schumacher, R. S., Galarneau, T. J., Jr., and Bosart, L. F.: Distant effects of a recurving tropical cyclones on rainfall in a midlatitude convective system: A high-impact predecessor rain event. Mon. Weather Rev., 139, 650-667, 2011.

Segami, A., Kurihara, K., Nakamura, H., Ueno, M., Takano, I., and Tatsumi, Y.: Operational mesoscale weather prediction with Japan Spectral Model, J. Meteor. Soc. Jpn., 67, 907-924, 1989.

Stevenson, S. N., and Schumacher, R. S.: A 10-year survey of extreme rainfall events in the central and eastern United States using gridded multisensor precipitation analyses, Mon. Weather Rev., 142, 3147-3162, 2014.

Sun, J., and Lee, T.-Y.: A numerical study of an intense quasi-stationary convection band over the Korean Peninsula, J. Meteor. Soc. Jpn., 80, 1221-1245, 2002.

Tompkins, A. M.: Organization of tropical convection in low vertical wind shears: The role of cold pools, J. Atmos. Sci., 58, 1650-1672, 2001.

Tsuboki, K., and Sakakibara, A.: Large-scale parallel computing of cloud resolving storm simulator, in: High Performance Computing, edited by: Zima, H. P., Joe, K., Sato, M., Seo, Y., and Shimasaki, M., Springer-Verlag, Berlin and Heidelberg, Germany; New York, NY, USA, ISBN: 978-3-540-47847-8, 243-259, 2002.

Tsuboki, K., and Sakakibara, A.: Numerical Prediction of High-Impact Weather Systems: the Textbook for the Seventeenth IHP Training Course in 2007, Hydrospheric Atmospheric Research Center, Nagoya University and UNESCO, Nagoya, Japan, ISBN: 978-4-9980619-8-4, 273 pp, 2007.

Wang, C.-C.: The more rain, the better the model performs---The dependency of quantitative precipitation forecast skill on rainfall amount for typhoons in Taiwan, Mon. Weather Rev., 143, 1723-1748, 2015.

Wang, C.-C.: Paper of notes: The more rain from typhoons, the better the models perform. Bull. Amer. Meteor. Soc., 97, 16-17, 2016.

Wang, C.-C., and Chen, G. T.-J.: Case study of the leeside mesolow and mesocyclone in TAMEX. Mon. Weather Rev., 130, 2572-2592.

Wang, C.-C., and Huang, W.-M.: High-resolution simulation of a nocturnal narrow convective line off the southeastern coast of Taiwan in the mei-yu season, Geophys. Res. Lett., 36, L06815, doi:10.1029/2008GL037147, 2009.

Wang, C.-C., Chen, G. T.-J., Chen, T.-C., and Tsuboki, K.: A numerical study on the effects of Taiwan topography on a convective line during the mei-yu season, Mon. Weather Rev., 133, 3217-3242, 2005.

Wang, C.-C., Chen, G. T.-J., and Huang, S.-Y.: Remote trigger of deep convection by cold outflow over the Taiwan Strait in the Mei-yu season: A modeling study of the 8 June 2007 case, Mon. Weather Rev., 139, 2854-2875, 2011.

Wang, C.-C., Kuo, H.-C., Chen, Y.-H., Huang, H.-L., Chung, C.-H., and Tsuboki, K.: Effects of asymmetric latent heating on typhoon movement crossing Taiwan: The case of Morakot (2009) with extreme rainfall, J. Atmos. Sci., 69, 3172-3196, 2012.

Wang, C.-C., Kuo, H.-C., Yeh, T.-C., Chung, C.-H., Chen, Y.-H., Huang, S.-Y., Wang, Y.-W., and Liu, C.-H.: High-resolution quantitative precipitation forecasts and simulations by the Cloud-Resolving Storm Simulator (CReSS) for Typhoon Morakot (2009), J. Hydrol., 506, 26-41, http://dx.doi.org/10.1016/j.jhydrol.2013.02.018, 2013.

Wang, C.-C., Hsu, J. C.-S., Chen, G. T.-J., and Lee, D.-I.: A study of two propagating heavy-rainfall episodes near Taiwan during SoWMEX/TiMREX IOP-8 in June 2008. Part I: Synoptic evolution, episode propagation, and model control simulation, Mon. Weather Rev., 142, 2619-2643, 2014a.

Wang, C.-C., Hsu, J. C.-S., Chen, G. T.-J., and Lee, D.-I.: A study of two propagating heavy-rainfall episodes near Taiwan during SoWMEX/TiMREX IOP-8 in June 2008. Part II: Sensitivity tests on the roles of synoptic conditions and topographic effects, Mon. Weather Rev., 142, 2644-2664, 2014b.

Wang, C.-C., Kuo, H.-C., Johnson, R.-H., Lee, C.-Y., Huang, S.-Y., and Chen, Y.-H.: A numerical study of convection in rainbands of Typhoon Morakot (2009) with extreme

rainfall: Roles of pressure perturbations with low-level wind maxima, Atmos. Chem. Phys., 15, 11097-11115, doi:10.5194/acp-15-11097-2015, 2015.

Wang, C.-C., Huang, S.-Y., Chen, S.-H., Chang, C.-S., and Tsuboki, K.: Cloud-resolving typhoon rainfall ensemble forecasts for Taiwan with large domain and extended range through time-lagged approach, Weather Forecast., 31, 151-172, 2016a.

Wang, C.-C., Chen, G. T.-J., and Ho, K.-H.: A diagnostic case study of mei-yu frontal retreat and associated low development near Taiwan. Mon. Weather Rev., 144, 2327-2349, 2016b.

Wang, H., Luo, Y.-L., and Jou, B. J.-D.: Initiation, maintenance, and properties of convection in an extreme rainfall event during SCMREX: observational analysis, J. Geophys. Res. Atmos., 119: 13206-13232, doi: 10.1002/2014JD022339, 2014.

Weisman, M. L., and Klemp, J. B.: Characteristics of isolated convective storms, in: Mesoscale Meteorology and Forecasting, edited by: Ray, P. S., Am. Meteor. Soc., Boston, MA, USA, 331-358, 1986.

Weisman, M. L., and Rotunno, R.: "A theory for strong long-lived squall lines" revisited, J. Atmos. Sci., 61, 361-382, 2004.

Wilhelmson, R. B., and Ogura, Y.: The pressure perturbation and the numerical modeling of a cloud, J. Atmos. Sci., 29, 1295-1307, 1972.

Xu, W., Zipser, E. J., Chen, Y.-L., Liu, C., Liou, Y.-C., Lee, W.-C., and Jou, B. J.-D.: An orography-associated extreme rainfall event during TiMREX: Initiation, storm evolution, and maintenance, Mon. Weather Rev., 140, 2555-2574, 2012.

Yang, M.-J., and Houze, R. A., Jr.: Multicell squall-line structure as a manifestation of vertically trapped gravity waves. Mon. Weather Rev., 123, 641-661, 1995.

Yeh, H.-C., and Chen, Y.-L.: The role of offshore convergence on coastal rainfall during TAMEX IOP 3, Mon. Weather Rev., 130, 2709-2730, 2002.

Yu, C.-K., and Chen, Y.: Surface fluctuations associated with tropical cyclone rainbands observed near Taiwan during 2000-08, J. Atmos. Sci., 68, 1568-1585, 2011.

Zhang, M., and Zhang, D.-L.: Subkilometer simulation of a torrential-rain-producing mesoscale convective system in East China. Part I: Model verification and convective organization, Mon. Weather Rev., 140, 184-201, 2012.

1   Table 1. The CReSS model domain configuration and physics used in this study.

2

Projection	Lambert Conformal (center at 120°E, secant at 10°N and 40°N)
Grid spacing	1.5 km × 1.5 km × 100-980 m (400 m)*
Dimension and size (x, y, z)	1000 × 800 × 50 (1500 km × 1200 km × 20 km)
IC/BCs	NCEP 0.5° × 0.5° analyses (26 levels, every 6 h)
Topography and SST	Real at (1/120)° and weekly mean on 1° × 1° grid
Integration period	1200 UTC 10 Jun to 1200 UTC 12 Jun 2012 (48 h)
Output frequency	Every 15 min (every 5 min during 1800-2400 UTC 11 Jun)
Cloud microphysics	Bulk cold-rain scheme (6 species)
PBL parameterization	1.5-order closure with prediction of turbulent kinetic energy
Surface processes	Energy/momentum fluxes, shortwave and longwave radiation
Substrate soil model	41 levels, every 5 cm to 2m deep

3   * The vertical grid spacing (Δz) of CReSS is stretched (smallest at the bottom), and the

4   averaged spacing is given in the parentheses.

5

2 Figure 1. CWB surface analyses and positions of front/trough (or wind-shift line, thick dashed)

3 at 850 (red), 700 (blue), 500 (green), and 200 hPa (orange) at 12:00 UTC 11 Jun 2012. The

4 CReSS model domain is marked by the dotted box.

5 Figure 2. (a) NCEP (0.5°) 950 hPa analysis and (b) CReSS simulation of horizontal winds (m

6 s^{-1}, speed shaded, scale to the right) at $z = 549$ m at 12:00 UTC 11 Jun 2012, with frontal

7 position marked (thick dashed lines). (c, d) Frontal positions every 6 h from 06:00 UTC 11

8 Jun to 12:00 UTC 12 Jun 2012 (c) at 950 hPa in NCEP analyses and (d) at $z = 549$ m in model

9 (see legend for line color and style), overlaid with topography (km, shading, scale to the right).

10 The triangle in (c) marks the location of Panchiao sounding in Fig. 3. (e, f) ASCAT oceanic

11 winds (m s^{-1}) near Taiwan at (e) 13:00 UTC 11 Jun and (f) 02:00 UTC 12 Jun, 2012, with

12 surface frontal position analyzed.

13 Figure 3. Thermodynamic (skew T-log p) diagram for the sounding taken at Panchiao (46692,

14 cf. Fig. 2c for location) at 12:00 UTC 11 Jun 2012. For winds, full (half) barbs denote 10 (5)

15 kts (1 kt = 0.5144 m s^{-1}), respectively.

16 Figure 4. Composite VMI radar reflectivity (dBZ, color, scale to the right) over the Taiwan

17 area at 1 h intervals from (a) 12:00 UTC 11 Jun to (i) 02:00 UTC 12 Jun, 2012. The outline of

18 Taiwan is highlighted (thick dotted lines) and the surface frontal position is plotted at synoptic

19 times (thick dashed lines).

20 Figure 5. Distribution of observed 6-h accumulated rainfall (mm, color, scale to the right)

21 over Taiwan during (a) 12:00-18:00 UTC and (b) 18:00-24:00 UTC 11 Jun 2012. The Taipei

22 City boundary is depicted in panel (a), and the dotted box in (b) shows the region used in Fig.

23 8 for rainfall average. (c, d) As in (a, b), but showing model-simulated rainfall over Taiwan

24 and the surrounding oceans.

25 Figure 6. As in Fig. 4, but showing reflectivity over northern Taiwan and the upstream area

26 every 10 min from (a) 19:40 UTC to (o) 22:00 UTC 11 Jun 2012 using a different set of

27 colors. The arrows mark the initiation or strengthening of back-building cells, off the western

28 end of a rainband or upstream from an old cell.

29 Figure 7. CReSS simulation of surface winds at 10 m height (m s^{-1}) and column-maximum

30 mixing ratio of precipitation (rain + snow + graupel, g kg^{-1}, shading, scale to the right) every

2 h from (a) 12:00 UTC to (f) 22:00 UTC 11 Jun 2012. For winds, full (half) barbs denote 10 (5) m s^{-1}, and the surface frontal positions are marked (thick dashed lines). The rectangle in panel (a) depicts the area (24.75-25.15°N, 120.35-121.75°E) used for the separation method.

Figure 8. Time series of observed (gray bars) and simulated (curve with dots) hourly rainfall (mm), averaged inside the box shown in Fig. 5b (24.75-25.17°N, 120.87-121.85°E) over northern Taiwan from 12:00 UTC 11 Jun to 06:00 UTC 12 Jun 2012.

Figure 9. CReSS simulation of horizontal winds (m s^{-1}, vectors, reference length at bottom) and convergence/divergence (10^{-4} s^{-1}, shading, scale to the right, positive for convergence) at 312-m height (contoured in thick gray) every 30 min from (a) 18:30 UTC to (f) 21:00 UTC 11 Jun 2012. The frontal positions (black dotted lines), and convergence axis (green dotted lines) and convective cells of interests are marked.

Figure 10. Model-simulated column-maximum vertical velocity (w, m s^{-1}, color and thin contours) every 10 min during 19:20-22:10 UTC 11 Jun 2012, overlaid with terrain elevation (m, thick contours at 250 and 500 m) in northern Taiwan. The color scale is shown at the bottom, and the contour at 0.5 m s^{-1} is not drawn. Old cells (A1, B1, and C1) and nearby new cells (A2, B2) of interests are labeled. Green dashed lines AB and CD depict the vertical cross-sections used in Fig. 11, and the short segments depict those used in Figs. 14-18 (blue (brown) ones through B1 (C1)).

Figure 11. (a) E-W vertical cross-section of model-simulated convergence/divergence (10^{-4} s^{-1}, color, positive for convergence) and θ_e (K, contour, every 1 K) along 25°N (line AB in Fig. 10), averaged over 21:25-21:35 UTC 11 Jun 2012. The triangle marks the mean location of the updraft of B1. (b, c) As in panel (a), except showing (b) convergence/divergence (color) and wind vectors (m s^{-1}) and speed (isotach every 1 m s^{-1}) and (c) w (m s^{-1}, color) and vertical wind shear vector (10^{-3} s^{-1}, in cordinal direction, reference vectors both plotted) along the WSW-ENE section (line CD in Fig. 10) at 21:00 UTC 11 Jun 2012. Thick arrow-lines in (b, c) depict the axis of the LLJ.

Figure 12. CReSS simulation of convergence/divergence (10^{-4} s^{-1}, shading, scale to the right, positive for convergence), 10-m wind perturbation (m s^{-1}, green vectors, reference length at bottom), and potential temperature perturbation (θ', K, contours every 0.1 K, dashed for negative values) at the surface every 20 min from (a) 20:00 UTC to (f) 21:00 UTC 11 Jun 2012. Cells B1 (black) and B2 (blue), axis of convergence (thick dotted line) produced by

32

Figure 13. Model-simulated w (m s^{-1}, color, scale at bottom) and laplacian of perturbation pressure (10^{-6} Pa m^{-2}, contour, every 3×10^{-6} Pa m^{-2}, dashed for negative values) of cells B1 and B2 at (left) 806 m and (right) 2929 m at 21:00 UTC 11 Jun 2012. (a, d) $\nabla^2 p'$ obtained from separation method, and (b, e) $\nabla^2 p' = \nabla^2 p'_b + \nabla^2 p'_d$ and (c, f) $\nabla^2 p'_b$ computed from Eqs. (3) and (4). Cells B1 and B2 and updraft and downdraft centers are labeled in panels (a) and (d).

Figure 14. Vertical cross-sections of model-simulated w (m s^{-1}, color) and (a) $\nabla^2 p'$ (10^{-6} Pa m^{-2}) and wind vectors (m s^{-1}, reference vector at bottom) on section plain, (b) $\nabla^2 p'_b$ (computed from Eq. 3), and (c) $\nabla^2 p'_d$ (computed from Eq. 4) and vertical wind shear vector (10^{-3} s^{-1}, in cardinal direction, reference vector at bottom) along the E-W segment through B1 and B2 at 20:00 UTC 11 Jun 2012 (cf. Fig. 10). All contour intervals are 3×10^{-6} Pa m^{-2} (zero line omitted, dashed for negative values), and letters H (L) denote corresponding high (low) pressure perturbations. (d-f), (g-i), and (j-l) As in (a-c), except at 20:20, 20:40, 21:00 UTC (WNW-ESE segments for 20:40 and 21:00 UTC, cf. Fig. 10), respectively.

Figure 15. (a-c) As in Fig. 14a-c, but showing w and (a) buoyancy B (10^{-3} m s^{-2}, black contour) and mixing ratio of cloud particles (g kg^{-1}, blue contour, every 3 g kg^{-1}), (b) $g(\theta'_v/\theta_{v0})$ (10^{-3} m s^{-2}), and (c) $-g\sum q_x$ (10^{-3} m s^{-2}). All black contour intervals are 3×10^{-6} Pa m^{-2} (dashed for negative values, zero line omitted), and + (−) signs denote upward (downward) maxima. (d-f), (g-i), and (j-l) As in (a-c), except at 20:20, 20:40, and 21:00 UTC, respectively.

Figure 16. As in Fig. 14, but showing w and (a, d, g) $p' = p'_b + p'_d$ (Pa, black contour, every 10 Pa, dashed for negative values) obtained from the rexalation method and the corresponding perturbation PGF in the vertical ($-(\partial p'/\partial z)/\rho_0$, 10^{-3} m s^{-2}, blue contour), (b, e, h) p'_b (Pa) and its vertical PGF (10^{-3} m s^{-2}), and (c, f, i) dw/dt from vertical perturbation PGF and B (10^{-3} m s^{-2}, black contour). For force (per unit mass) and acceleration, all contour intervals are 5×10^{-3} m s^{-2} (dashed for negative values), and upward (downward) arrows denote maxima (minima).

Figure 17. As in Fig. 14, but showing w (m s^{-1}, color) and (a) $\nabla^2 p'$ (10^{-6} Pa m^{-2}) and wind vectors (m s^{-1}) on section plain, (b) $\nabla^2 p'_b$, and (c) $\nabla^2 p'_d$ and vertical wind shear vector (10^{-3} s^{-1}, in cardinal direction) along the WSW-ENE segment through C1 at 20:40 UTC 11 Jun 2012 (cf. Fig. 10). (d-f) As in (a-c), except at 21:20 UTC.

Figure 18. (a, b) As in Fig. 15a and b, but showing w (color) and (a) B (black contour) and mixing ratio of cloud particles (blue contour) and (b) $g(\theta'_v/\theta_{v0})$ along the WSW-ENE segment through C1 at 21:20 UTC 11 Jun 2012. (c, d) As in Fig. 16a and b, but showing w and (c) p' (black contour) obtain from the relaxation method and $-(\partial p'/\partial z)/\rho_0$ (blue contour) and (d) p'_b and its vertical PGF along the segment as in panels (a, b) at 21:20 UTC.

Figure 1. CWB surface analyses and positions of front/trough (or wind-shift line, thick dashed) at 850 (red), 700 (blue), 500 (green), and 200 hPa (orange) at 12:00 UTC 11 Jun 2012. The CReSS model domain is marked by the dotted box.

Figure 2. (a) NCEP (0.5°) 950 hPa analysis and (b) CReSS simulation of horizontal winds (m

s^{-1}, speed shaded, scale to the right) at z = 549 m at 12:00 UTC 11 Jun 2012, with frontal

position marked (thick dashed lines). (c, d) Frontal positions every 6 h from 06:00 UTC 11

1 Jun to 12:00 UTC 12 Jun 2012 (c) at 950 hPa in NCEP analyses and (d) at $z = 549$ m in model

2 (see legend for line color and style), overlaid with topography (km, shading, scale to the right).

3 The triangle in (c) marks the location of Panchiao sounding in Fig. 3. (e, f) ASCAT oceanic

4 winds (m s^{-1}) near Taiwan at (e) 13:00 UTC 11 Jun and (f) 02:00 UTC 12 Jun, 2012, with

5 surface frontal position analyzed.
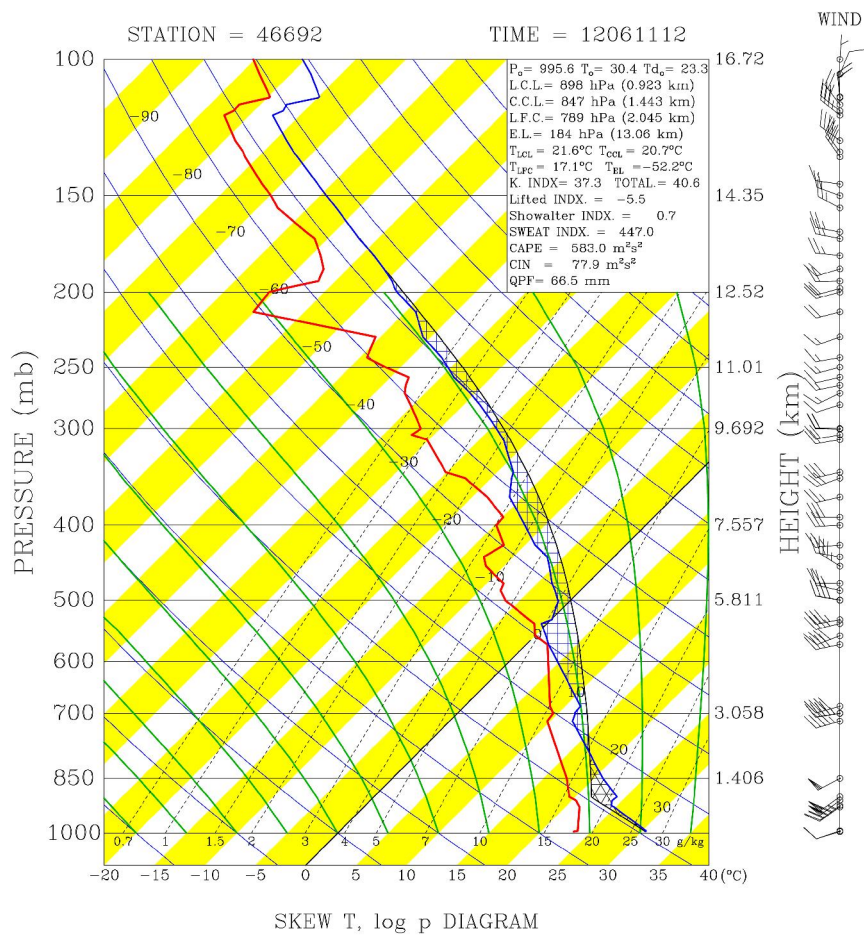
Figure 3. Thermodynamic (skew *T*-log *p*) diagram for the sounding taken at Panchiao (46692, cf. Fig. 2c for location) at 12:00 UTC 11 Jun 2012. For winds, full (half) barbs denote 10 (5) kts (1 kt = 0.5144 m s^{-1}), respectively.
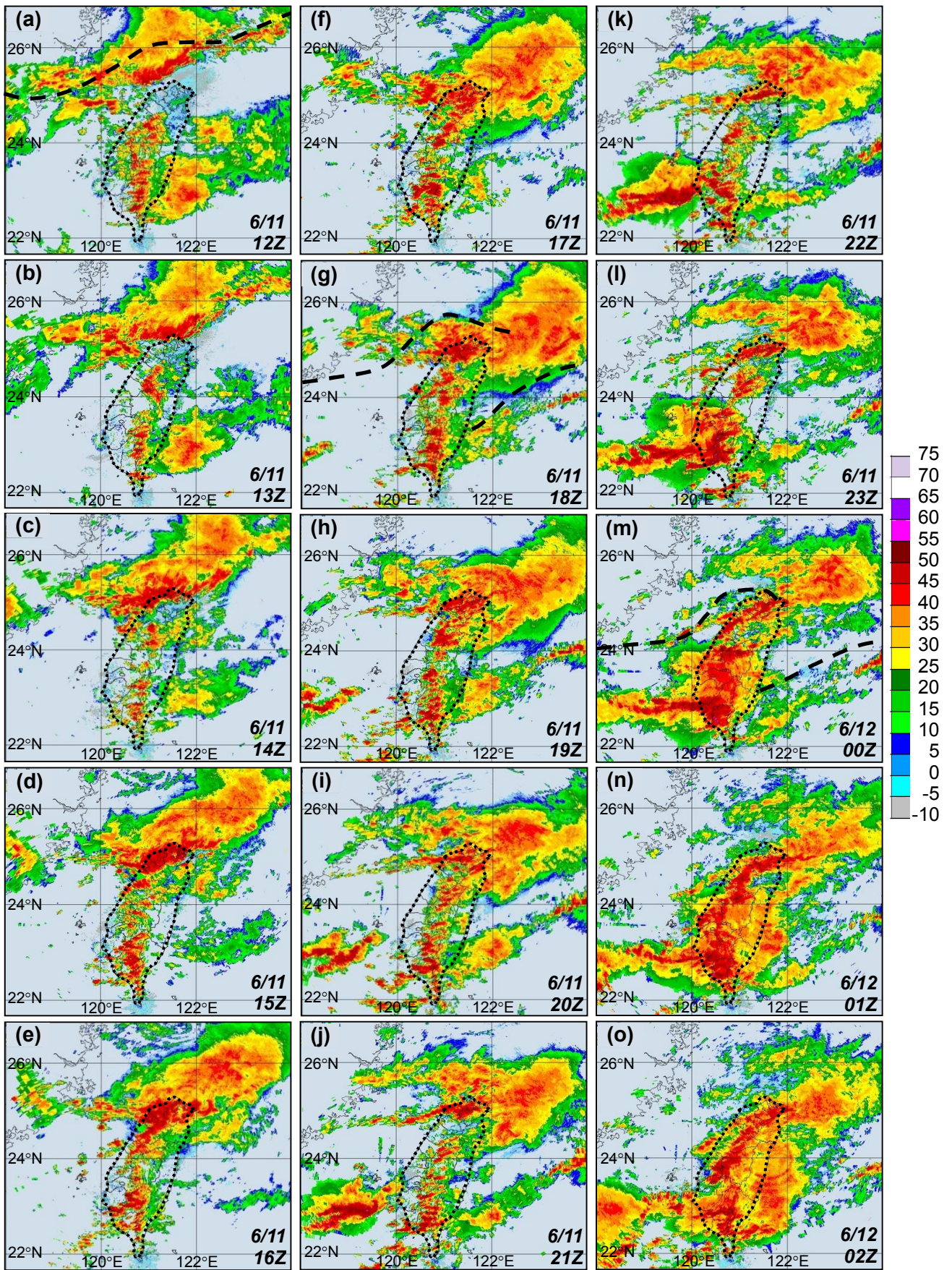
1   Figure 4. Composite VMI radar reflectivity (dBZ, color, scale to the right) over the Taiwan

2   area at 1-h intervals from (a) 1200 UTC 11 Jun to (i) 0200 UTC 12 Jun, 2012. The outline of

3   Taiwan is highlighted (thick dotted lines) and the surface frontal position is plotted at synoptic

4   times (thick dashed lines).

Figure 5. Distribution of observed 6-h accumulated rainfall (mm, color, scale to the right) over Taiwan during (a) 12:00-18:00 UTC and (b) 18:00-24:00 UTC 11 Jun 2012. The Taipei City boundary is depicted in panel (a), and the dotted box in (b) shows the region used in Fig. 9 for rainfall average. (c, d) As in (a, b), but showing model-simulated rainfall over Taiwan and the surrounding oceans.

Figure 6. As in Fig. 4, but showing reflectivity over northern Taiwan and the upstream area every 10 min from (a) 19:40 UTC to (o) 22:00 UTC 11 Jun 2012 using a different set of colors. The arrows mark the initiation or strengthening of back-building cells, off the western end of a rainband or upstream from an old cell.

Figure 7. CReSS simulation of surface winds at 10 m height (m s^{-1}) and column-maximum

mixing ratio of precipitation (rain + snow + graupel, g kg^{-1}, shading, scale to the right) every

1   2 h from (a) 12:00 UTC to (f) 22:00 UTC 11 Jun 2012. For winds, full (half) barbs denote 10

2   (5) m s^{-1}, and the surface frontal positions are marked (thick dashed lines). The rectangle in

3   panel (a) depicts the area (24.75-25.15°N, 120.35-121.75°E) used for the separation method.
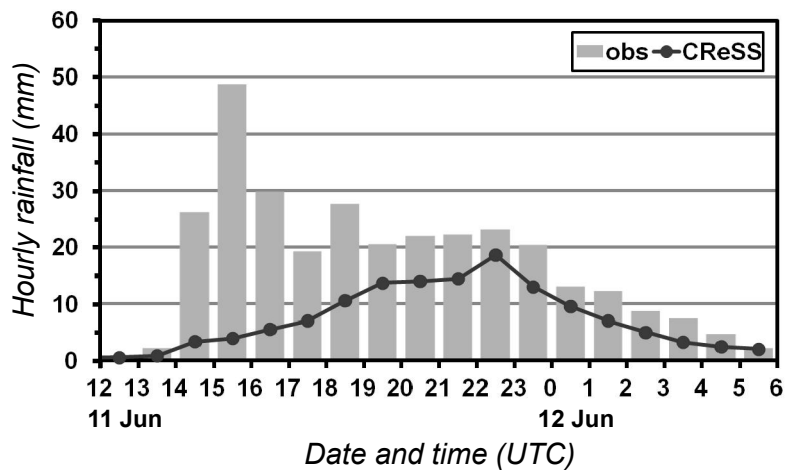
1　Figure 8. Time series of observed (gray bars) and simulated (curve with dots) hourly rainfall

2　(mm), averaged inside the box shown in Fig. 5b (24.75-25.17°N, 120.87-121.85°E) over

3　northern Taiwan from 12:00 UTC 11 Jun to 06:00 UTC 12 Jun 2012.
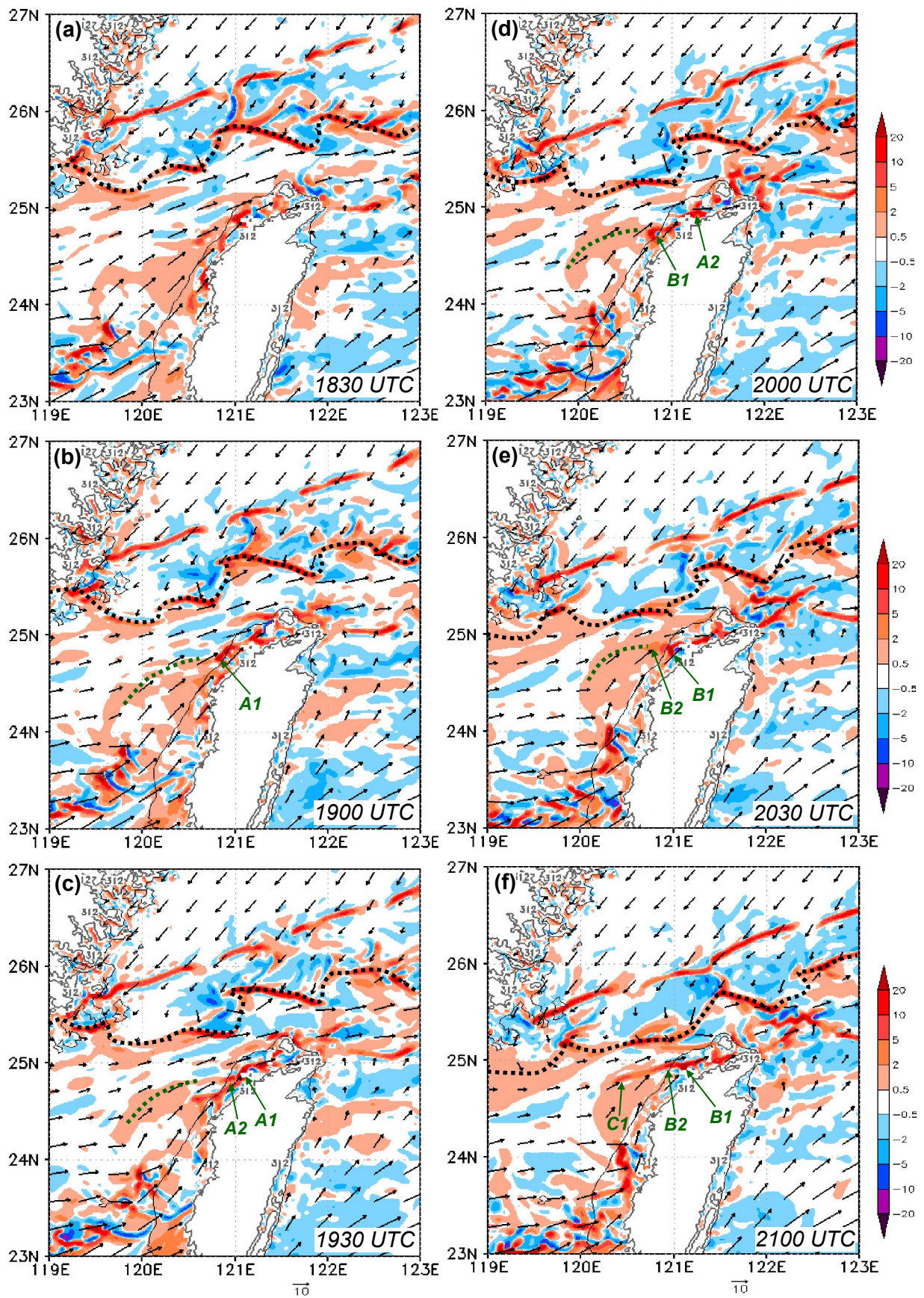
1   Figure 9. CReSS simulation of horizontal winds (m s^{-1}, vectors, reference length at bottom)

1 and convergence/divergence (10^{-4} s^{-1}, shading, scale to the right, positive for convergence) at

2 312-m height (contoured in thick gray) every 30 min from (a) 18:30 UTC to (f) 21:00 UTC 11

3 Jun 2012. The frontal positions (black dotted lines), and convergence axis (green dotted lines)

4 and convective cells of interests are marked.

Figure 10. Model-simulated column-maximum vertical velocity (w, m s^{-1}, color and thin contours) every 10 min during 19:20-22:10 UTC 11 Jun 2012, overlaid with terrain elevation (m, thick contours at 250 and 500 m) in northern Taiwan. The color scale is shown at the bottom, and the contour at 0.5 m s^{-1} is not drawn. Old cells (A1, B1, and C1) and nearby new cells (A2, B2) of interests are labeled. Green dashed lines AB and CD depict the vertical cross-sections used in Fig. 11, and the short segments depict those used in Figs. 14-18 (blue (brown) ones through B1 (C1)).

Figure 11. (a) E-W vertical cross-section of model-simulated convergence/divergence (10^{-4} s^{-1}, color, positive for convergence) and θ_e (K, contour, every 1 K) along 25°N (line AB in Fig. 10), averaged over 21:25-21:35 UTC 11 Jun 2012. The triangle marks the mean location of the updraft of B1. (b, c) As in panel (a), except showing (b) convergence/divergence (color) and wind vectors (m s^{-1}) and speed (isotach every 1 m s^{-1}) and (c) w (m s^{-1}, color) and vertical wind shear vector (10^{-3} s^{-1}, in cordinal direction, reference vectors both plotted) along the WSW-ENE section (line CD in Fig. 10) at 21:00 UTC 11 Jun 2012. Thick arrow-lines in (b, c) depict the axis of the LLJ.

Figure 12. CReSS simulation of convergence/divergence (10^{-4} s^{-1}, shading, scale to the right, positive for convergence), 10-m wind perturbation (m s^{-1}, green vectors, reference length at bottom), and potential temperature perturbation (θ', K, contours every 0.1 K, dashed for negative values) at the surface every 20 min from (a) 20:00 UTC to (f) 21:00 UTC 11 Jun 2012. Cells B1 (black) and B2 (blue), axis of convergence (thick dotted line) produced by downdraft outflow of B1, and locations of vertical cross sections as in Fig. 10 (straight dashed lines) are marked.
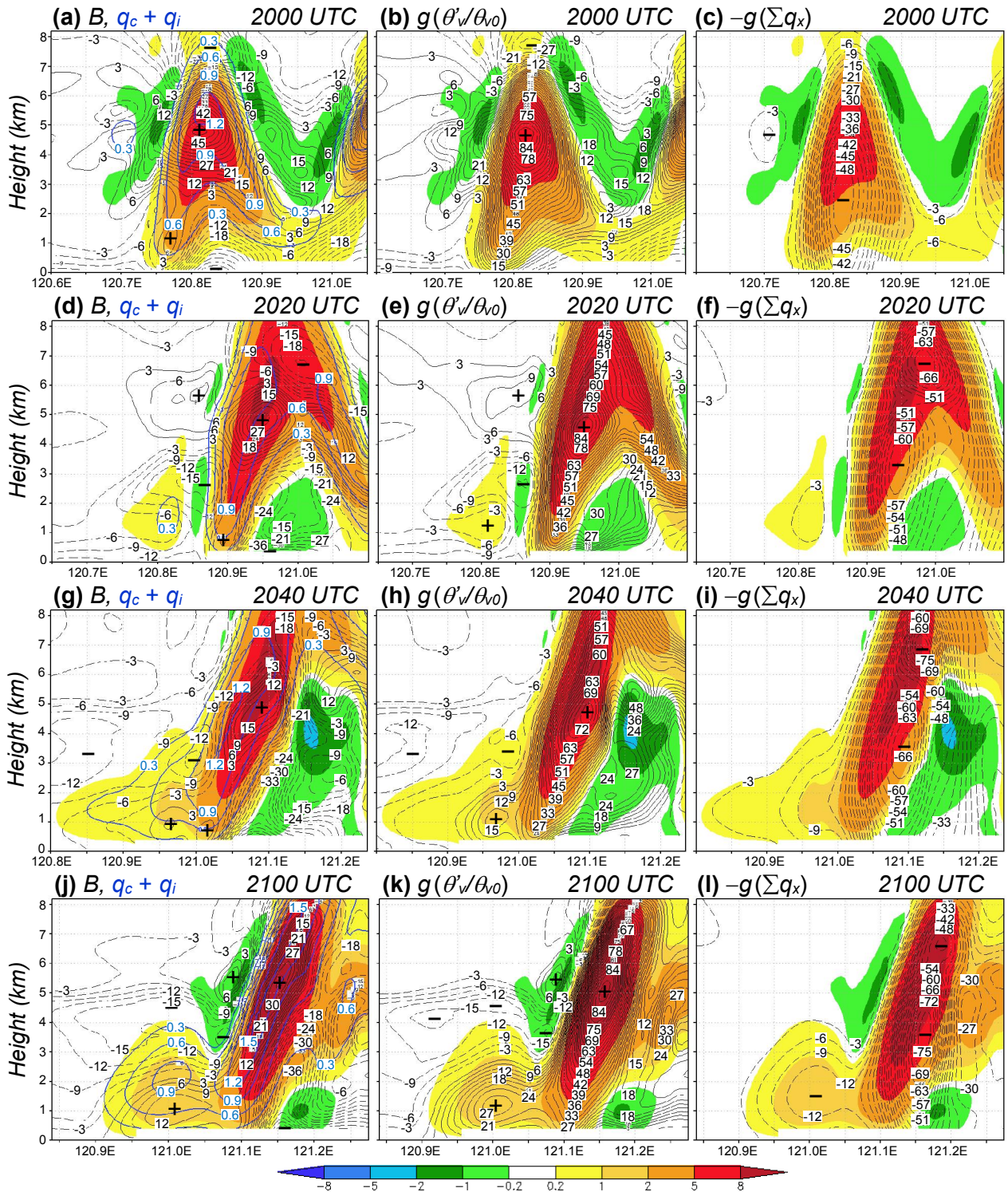
Figure 13. Model-simulated w (m s^{-1}, color, scale at bottom) and laplacian of perturbation pressure (10^{-6} Pa m^{-2}, contour, every 3×10^{-6} Pa m^{-2}, dashed for negative values) of cells B1 and B2 at (left) 806 m and (right) 2929 m at 21:00 UTC 11 Jun 2012. (a, d) $\nabla^2 p'$ obtained from separation method, and (b, e) $\nabla^2 p' = \nabla^2 p'_b + \nabla^2 p'_d$ and (c, f) $\nabla^2 p'_b$ computed from Eqs. (3) and (4). Cells B1 and B2 and updraft and downdraft centers are labeled in panels (a) and (d).
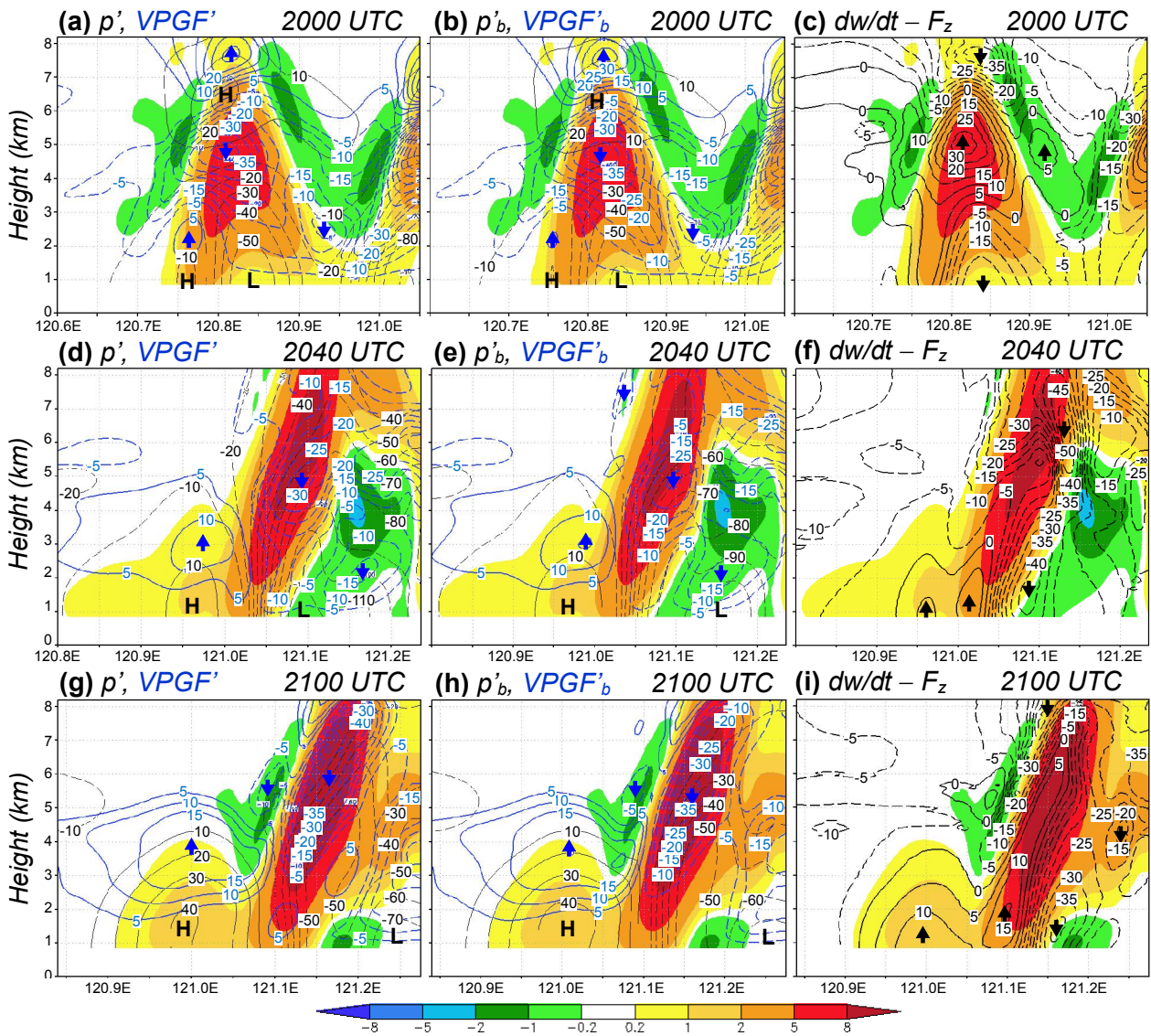
Figure 14. Vertical cross-sections of model-simulated w (m s^{-1}, color) and (a) $\nabla^2 p'$ (10^{-6} Pa m^{-2}) and wind vectors (m s^{-1}, reference vector at bottom) on section plain, (b) $\nabla^2 p'_b$ (computed from Eq. 3), and (c) $\nabla^2 p'_d$ (computed from Eq. 4) and vertical wind shear vector (10^{-3} s^{-1}, in cardinal direction, reference vector at bottom) along the E-W segment through B1 and B2 at 2000 UTC 11 Jun 2012 (cf. Fig. 10). All contour intervals are 3×10^{-6} Pa m^{-2} (zero
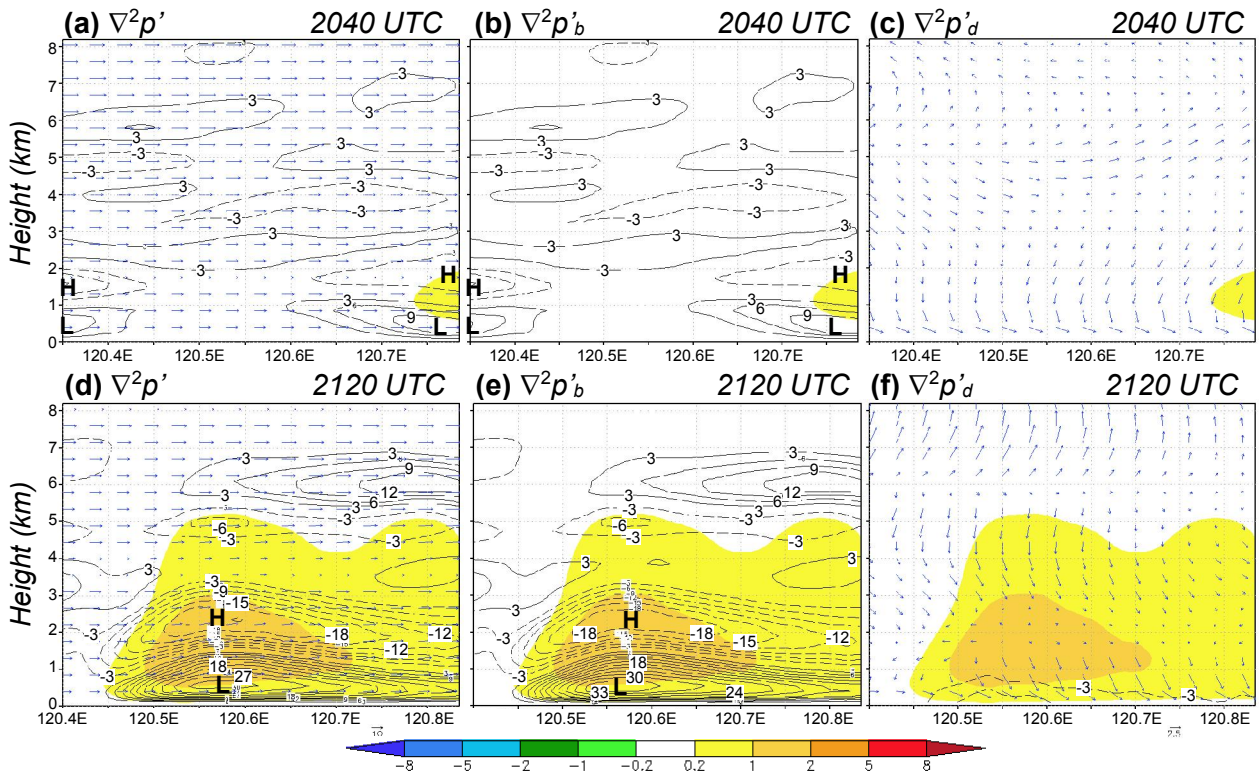
1   line omitted, dashed for negative values), and letters H (L) denote corresponding high (low)

2   pressure perturbations. (d-f), (g-i), and (j-l) As in (a-c), except at 20:20, 20:40, 21:00 UTC

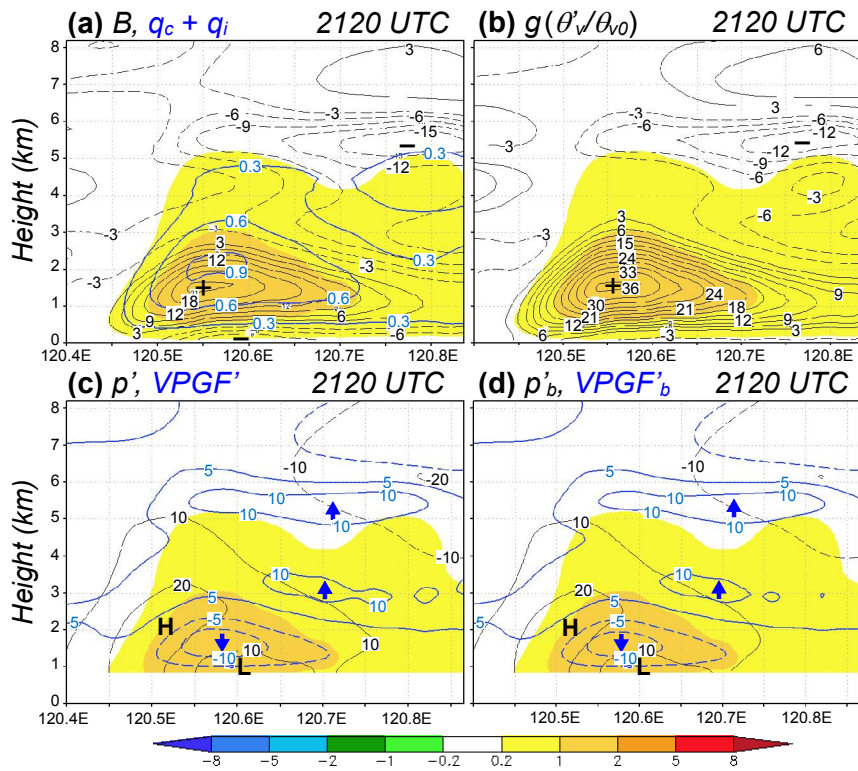3   (WNW-ESE segments for 20:40 and 21:00 UTC, cf. Fig. 10), respectively.

Figure 15. (a-c) As in Fig. 14a-c, but showing w and (a) buoyancy B (10^{-3} m s^{-2}, black contour) and mixing ratio of cloud particles (g kg^{-1}, blue contour, every 3 g kg^{-1}), (b) $g(\theta'_v/\theta_{v0})$ (10^{-3} m s^{-2}), and (c) $-g\sum q_x$ (10^{-3} m s^{-2}). All black contour intervals are 3×10^{-6} Pa m^{-2} (dashed for negative values, zero line omitted), and + (−) signs denote upward (downward) maxima. (d-f), (g-i), and (j-l) As in (a-c), except at 20:20, 20:40, and 21:00 UTC, respectively.

Figure 16. As in Fig. 14, but showing w and (a, d, g) $p' = p'_b + p'_d$ (Pa, black contour, every 10 Pa, dashed for negative values) obtained from the rexalation method and the corresponding perturbation PGF in the vertical ($-(\partial p'/\partial z)/\rho_0$, 10^{-3} m s^{-2}, blue contour), (b, e, h) p'_b (Pa) and its vertical PGF (10^{-3} m s^{-2}), and (c, f, i) dw/dt from vertical perturbation PGF and B (10^{-3} m s^{-2}, black contour). For force (per unit mass) and acceleration, all contour intervals are 5×10^{-3} m s^{-2} (dashed for negative values), and upward (downward) arrows denote maxima (minima).

Figure 17. As in Fig. 14, but showing w (m s^{-1}, color) and (a) $\nabla^2 p'$ (10^{-6} Pa m^{-2}) and wind vectors (m s^{-1}) on section plain, (b) $\nabla^2 p'_b$, and (c) $\nabla^2 p'_d$ and vertical wind shear vector (10^{-3} s^{-1}, in cardinal direction) along the WSW-ENE segment through C1 at 20:40 UTC 11 Jun 2012 (cf. Fig. 10). (d-f) As in (a-c), except at 21:20 UTC.

1   Figure 18. (a, b) As in Fig. 15a and b, but showing w (color) and (a) B (black contour) and

2   mixing ratio of cloud particles (blue contour) and (b) $g(\theta'_v/\theta_{v0})$ along the WSW-ENE segment

3   through C1 at 21:20 UTC 11 Jun 2012. (c, d) As in Fig. 16a and b, but showing w and (c) p'

4   (black contour) obtain from the relaxation method and $-(\partial p'/\partial z)/\rho_0$ (blue contour) and (d) p'_b

5   and its vertical PGF along the segment as in panels (a, b) at 21:20 UTC.